An in-silico proof-of-concept of electrohydrodynamic air amplifier for low-energy airflow generation

Donato Rubinetti [1,2], Kamran Iranshahi [1,3], Daniel Onwude[1], Lei Xie [4], Bart Nicolai [2], Thijs Defraeye [1,5] *

[1] *Empa, Swiss Federal Laboratories for Materials Science and Technology, Laboratory for Biomimetic Membranes and Textiles, Lerchenfeldstrasse 5, CH-9014 St. Gallen, Switzerland*

[2] *KU Leuven, Katholieke Universiteit Leuven, Faculty of Bioscience Engineering, Kasteelpark Arenberg 20, BE-3001 Leuven, Belgium*

[3] *ETH-Zurich, Swiss Federal Institute of Technology, Zurich 8092, Switzerland*

[4] *Belimed AG, Grienbachstrasse 11, CH-6300 Zug, Switzerland*

[5]*Dalhousie University, Faculty of Agriculture, Truro, Nova Scotia, Canada*

Using electrohydrodynamics (EHD) we can generate airflow without impellers or other moving parts. This airflow, or ionic wind, is invoked by corona discharge with the subsequent acceleration of electrically charged air molecules in a strong electric field. However, EHD-induced air propulsion is considered inefficient due to its low electrical to mechanical energy conversion rate compared to conventional fans. This study aims at improving the energy efficiency expressed in flow rate to electrical power input of EHD-based airflow devices. A novel bladeless air propulsion device is proposed that combines ionic wind with air amplification based on the Coanda phenomenon to amplify EHD-generated flow rates. We assess the performance of the bladeless air propulsion device as an alternative technology to conventional fans by investigating the fluid dynamics, electrostatics, and energy consumption. We demonstrate the proof-of-concept with an innovative fully-coupled simulation approach for corona discharge and EHD modeling. We explore different design parameters on the conceptual EHD air amplifier, such as the electric potential (10-30 kV) of the discharge electrode, the electrode spacing (5-25 mm), the channel height (30-150 mm). The studies are performed on a 2D constrained channel flow and a 2D-axisymmetric open space design, respectively. In order to quantify the benefit of air amplification on EHD, the results are benchmarked to a regular EHD setup without amplifying vane as well as to a comparable commercial axial fan. Regarding the energy efficiency measure of flow rate per electric power input, the EHD air amplifier in the constrained flow configuration improves the energy efficiency by 59% compared to regular EHD and by 48% compared to the axial fan. Amplification factors of 16.5 to 19 are achieved for the constrained configuration and 5.5 to 6.4 for the open space configuration. These results show that EHD air amplification is a promising way to generate airflow with low energy consumption. By air amplification, we can increase the airflow rates of EHD with a factor 10.

Keywords: Air propulsion, CFD, electrohydrodynamics, corona discharge, Ionic wind, Coanda effect

* *Corresponding author: thijs.defraeye@empa.ch Swiss Federal Laboratories for Materials Science and Technology, Laboratory for Biomimetic Membranes and Textiles, Lerchenfeldstrasse 5, CH-9014 St. Gallen, Switzerland*

List of symbols

Symbol	Meaning	SI Unit
AF	Amplification factor	-
b	Ion mobility	$m^2\ V^{-1}\ s^{-1}$
D	Inner diameter	m
D_{ion}	Ion diffusivity	$m^2\ s^{-1}$
D_0	Electric displacement vector	$C\ m^{-2}$
E	Electric field vector	$V\ m^{-1}$
E_0	Corona discharge onset field strength	$V\ m^{-1}$
E_e	Corona discharge onset field strength on electrode	$V\ m^{-1}$
F_q	Coulomb force	N
H	Channel height	m
I	Electric current	A
J	Current density	$A\ m^{-2}$
P_{el}	Electric power	W
p	Pressure	Pa
r_e	Emitter electrode curvature	m
u	Velocity field vector	$m\ s^{-1}$
$\bar{u}$	Average velocity	$m\ s^{-1}$
$\dot{V}$	Volume flow rate	$m^3\ s^{-1}$
$\dot{V}_{in}$	Inlet volume flow rate	$m^3\ s^{-1}$
$\dot{V}_{out}$	Outlet volume flow rate	$m^3\ s^{-1}$
W	Width of the channel	m
y^+	Dimensionless wall distance	-
γ	Flow rate per electrical power	$m^3\ h^{-1}\ W^{-1}$
δ	Emitter-collector distance	m
ε	Vane nozzle gap	m
ε_0	Vacuum permittivity	$F\ m^{-1}$
ε_r	Relative permittivity	$F\ m^{-1}$
μ	Dynamic viscosity of air	Pa s
ϕ	Electric potential	V
ϕ_1	Electric potential on emitter electrode	V
ρ	Density of air	$kg\ m^{-3}$
ρ_{el}	Space charge density	$C\ m^{-3}$
$\rho_{el,0}$	Initial space charge density on electrode	$C\ m^{-3}$
Ω	Computational domain	m^2
Ω_{PLA}	Computational subdomain for PLA enclosure	m^2
Ω_{air}	Computational subdomain of air	m^2

1 Introduction

From the cooling fans of small-scale electronic devices to large-scale passenger aircraft engines, rotating machinery is successfully used in our daily lives to move air. Electrohydrodynamics (EHD) is another way to move air without rotating or other moving parts. EHD-generated airflow, often referred to as ionic wind, is created by corona discharge between two electrodes. Corona discharge is a plasma zone that is created when the fluid such as air around a conductor gets ionized [1]. In an electric field, the charged air molecules accelerate under the influence of the Coulomb force and transfer momentum to the surrounding neutral air by collision. As a result, a macroscopic airflow emerges. The fundamentals of EHD airflow generation are well-known. However, air propulsion technology has rarely considered the ionic wind principle as a viable alternative, mainly because of the low electrical to mechanical energy conversion efficiency. The conversion efficiency from electrical to mechanical energy in EHD is about 1%, while commonly adopted fans achieve an efficiency of 60% [2].

Many different EHD energy efficiency enhancement techniques have been investigated. Noteworthy efficiency gains were obtained via the optimization of electrode arrangement [3], [4], a surface-enlarging nanomaterial coating of discharging electrodes [5], an array design of multiple 3D-printed individual EHD pumps [6] or via sequentially connected ionic wind blowers [7]. The optimization attempts predominantly target the EHD phenomenon's electrostatic part by studying various types of emitter and collector configurations [8]. Another approach intends to employ magnetic fields on top of electric fields to augment the acceleration with the Lorentz force [9], [10]. However, these studies did not achieve sufficient flow rates to position EHD as a viable airflow generation technology alternative to conventional fans. To fill this gap, we focus on improving efficient EHD-driven airflow by aerodynamic effects instead of improving the efficiency on the electrostatic end alone.

For this purpose, we numerically investigate the combination of EHD with the principle of air amplification using the Coanda effect. The Coanda effect is the tendency of a fluid flow to stay attached to a solid wall, preferably convex, and remain attached even when the guiding wall deviates from the initial flow direction due to pressure asymmetries [11], [12]. This principle can be used to amplify airflow rates by entrainment of the surrounding air. In practice, an EHD-generated airstream jet is directed towards a solid wall and a priori stagnant surrounding air volume accelerates as well. The accelerated air volume is driven by a pressure difference and requires no other air propulsion device, leading to an overall flow rate and energy conversion efficiency increase. We demonstrate a geometry featuring EHD and the Coanda effect in a 2D confined channel and a 2D-axisymmetric variant for the free flow case for the in-silico proof-of-concept. Because of the multiphysical nature of EHD and the complexity in combining with airflow amplification using the Coanda effect phenomenon, we developed an advanced single species modeling approach. This approach iteratively adjusts the initial space charge density on the emitting electrode. The advancement is employed via a Lagrange multiplier as the fitting parameter that satisfies the Peek-Kaptzov condition.

2 Materials and methods

This simulation strategy studies the EHD air amplification influence parameters of the vast design space such as wire radius, electrode spacing, operation voltage, channel height, and vane slit. The results of EHD air amplification are compared to regular EHD and a standard fan in terms of flow rate, power consumption and flow rate to electrical power ratio to benchmark the efficiency gain of combining EHD airflow with the Coanda effect. The simulation study is performed first on a constrained flow 150x150x500 mm^3 channel simplified to a 2D domain with a wire-type electrode. Then, a 2D-axisymmetric case for open space EHD air amplification is accordingly investigated and compared.

All simulations are performed using a two-dimensional (2D) and two-dimensional axisymmetric (2Da) model. The model accounts for electrostatics (corona discharge) and turbulent airflow (CFD) and is fully coupled. The discharge phenomenon is considered via a single-species approach within the air domain. This way, the ionized and charge-free air fractions are both represented as a continuum, with the space charge density being the relevant distinction variable. The details for boundary conditions, assumptions, and simulation parameters are highlighted in this section.

2.1 Couplings in electrohydrodynamic airflow

EHD airflow is a complex multiphysical process that couples electrostatics and fluid flow. Ions are produced by the emitter electrode and accelerated via Coulomb force in the drift region. In transition from the emitter electrode to the collector electrode, the ions collide with air molecules, thus, generating a macroscopic airflow. The electrostatic action is influenced by geometrical factors and inherent physical conditions, such as, the minimum electric field intensity around the emitter to initiate ionization which is called corona onset field strength. Figure 1 maps the most relevant couplings and influence factors involved in EHD airflow generation.

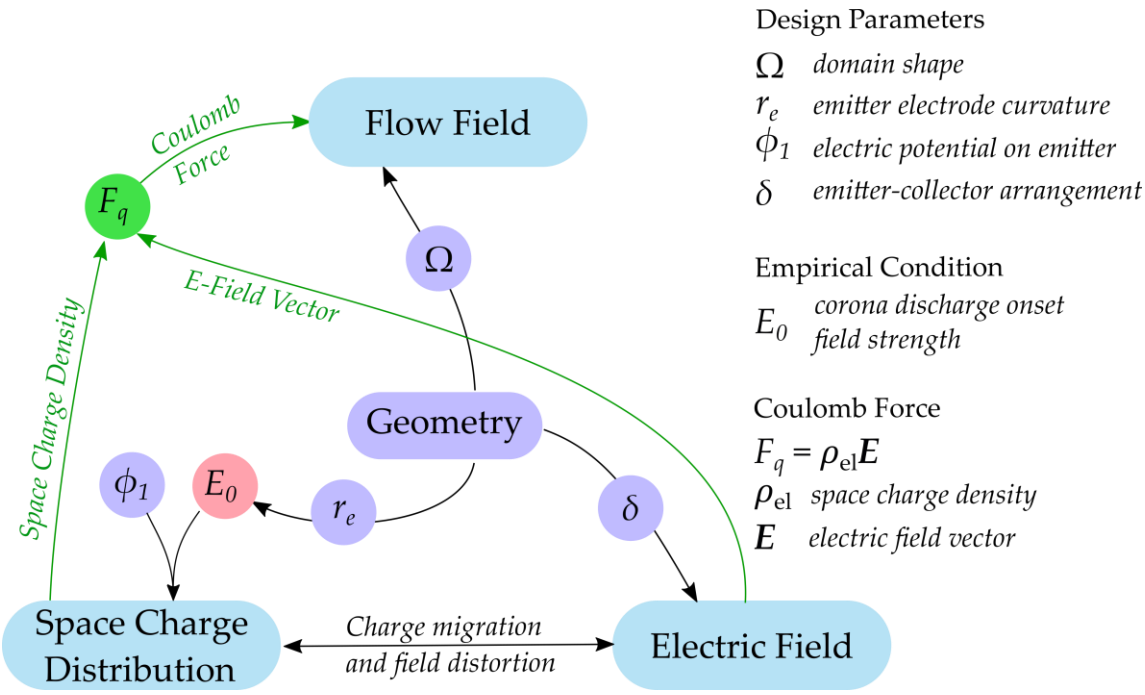

Figure 1: EHD airflow is a complex multiphysical phenomenon where the flow field establishes as a consequence of interactions between the space charge distribution and electric field. The geometry of the system provides the design parameters (purple) which highly influence all dependent fields (light blue; flow field, electric field, space charge distribution). Moreover, the production of charge is dependent on the onset field strength, an empirical condition (pink). From the electrostatic fields (space charge density and electric field) we obtain the Coulomb force, acting as body force onto the fluid and creating as a consequence a macroscopic airflow. This is a simplified representation of the multiphysical couplings and the design space of EHD airflow, which poses the basis for EHD air amplification. Simplified representation of multiphysical couplings and design space of EHD flow, which poses the basis for EHD air amplification.

EHD airflow itself is the consequence of the Coulomb force, which arises as a product of the electric field and space charge distribution. These two are highly influenced by several design parameters such as emitter electrode curvature, applied voltage on that electrode, and emitter-collector arrangement. Moreover, the electric field and space charge density interact by mutually influencing each other's distributions and intensities by charge migration and field distortion. As far as the electrostatic part of the problem is concerned, the emitter-collector arrangement, electrode shape, and the applied voltage are crucial design and tuning parameters.

2.2 EHD air amplification as combination of regular EHD with the Coanda effect

Linking EHD airflow with the Coanda effect results in EHD air amplification. In a first step, a regular EHD airstream is generated as by-product of corona discharge between two electrodes. This primary airstream is directed towards a nozzle, or, inlet and expanded on a nearby solid wall. The shape of the wall can be flat or convex. Due to one-sided pressure differences around the nozzle, the primary airstream is forced to remain attached to the solid wall. This causes the surrounding air to accelerate as well, thus, inducing a secondary airstream via air entrainment. The overall result is that the primary airstream is amplified without additional energy cost by means of the aerodynamical perks offered by the Coanda surface. The Coanda surface is the solid wall capable of expanding and attaching the primary airstream. Figure 3 and Figure 4 show principle sketches of EHD air amplification.

2.3 Geometrical configurations

Three different geometrical configurations are investigated based on the induced physics. The first is a regular EHD channel setup without air amplification that serves as benchmark. The second configuration is EHD with air amplification in a channel to investigate the principle and added value compared to regular EHD. Finally, an open space EHD air amplifier configuration is constructed to investigate whether flow confinement (in a channel) reduces the entrained flow by the Coanda effect. Commercially available fans employing air amplifier technology inspired the design of the amplifying geometries [13]. Irrespective of the enclosure shape, three components must always be present for EHD air amplification: (1) high voltage electrode, either a wire or a needle, or any other suitable sharp and strongly curved entity, (2) an enclosure where the electrodes are placed and a (3) Coanda surface. The enclosure is physically relevant to produce an EHD airstream separately and also to protect the outer environment from high voltage (HV) components.

2.3.1 Confined space regular EHD configuration (benchmark)

This simple 2D configuration serves as a benchmark where the electrode is placed within the confined space, and the corresponding ground varies in distance as seen in Figure 2. No air amplification occurs here, as the EHD-generated airflow itself is the main bulk flow within the channel.

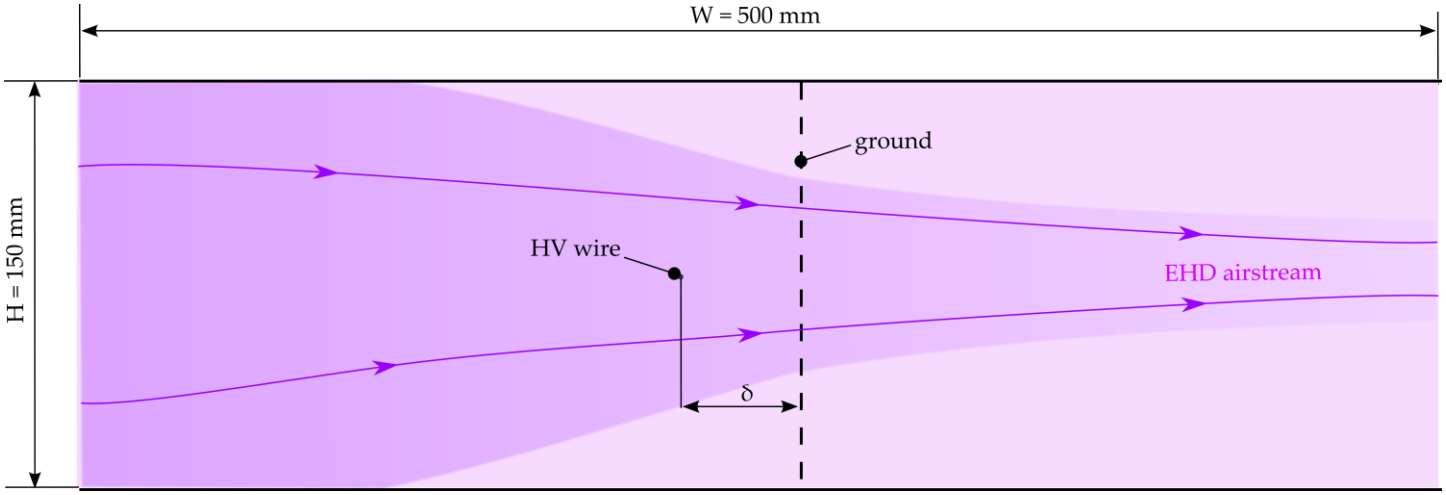

Figure 2: The confined space configuration of regular EHD without air amplification serves as benchmark. It includes a high voltage (HV) wire as emitter and a ground collector. The emitter-collector distance δ is variable.

2.3.2 EHD air amplification configuration in a confined space

This 2D configuration features an enclosure, also termed "vane," where the electrodes are placed inside, generating an EHD airstream as shown in Figure 3. Within the vane, a wire electrode with a radius r_e, which is used to start the corona discharge process, and a grounded mesh electrode with porosity 70 % are employed. A porosity of 70 % corresponds to a mesh structure with 1 mm wire diameter and 6 mm pitch. The spacing between wire and ground is δ. The EHD-generated airstream is pushed through a slit with gap width ε and is expected to remain attached to the Coanda surface. As a result, the Coanda effect is invoked, which drags the air of the channel leading to an amplified airstream.

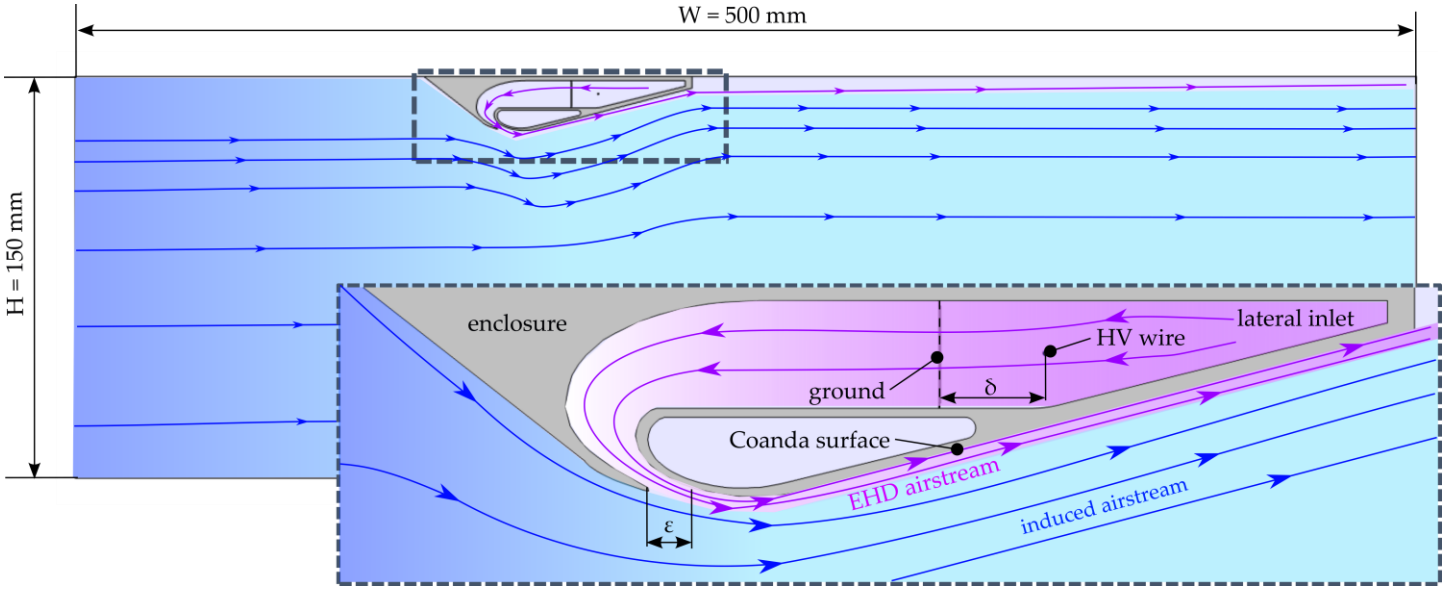

Figure 3: The confined space configuration of EHD air amplification features an enclosure (or, vane) which accommodates the electrical components. Within the enclosure a high voltage wire and ground act as accelerators of a primary airstream, e.g. the EHD airstream. This EHD airstream is pushed through a nozzle with gap size ε and remains attached to an inclined Coanda surface. As a result, a larger airflow is is induced which ultimately leads to the amplification of airflow rates

2.3.3 EHD air amplification configuration in open space

The third configuration is a 2D-axisymmetric geometry in open space. Here, we test the performance of EHD air amplification in an open room with a circular enclosure of inner diameter D. Like in the previous case, this configuration features the main components needed for EHD air amplification, i.e., electrodes, enclosure, and Coanda surface. The electrode, in this case, is again a wire which is circularly arranged within the enclosure with a spacing from the ground (δ). The corresponding ground counterpart is built into the slit with gap distance ε.

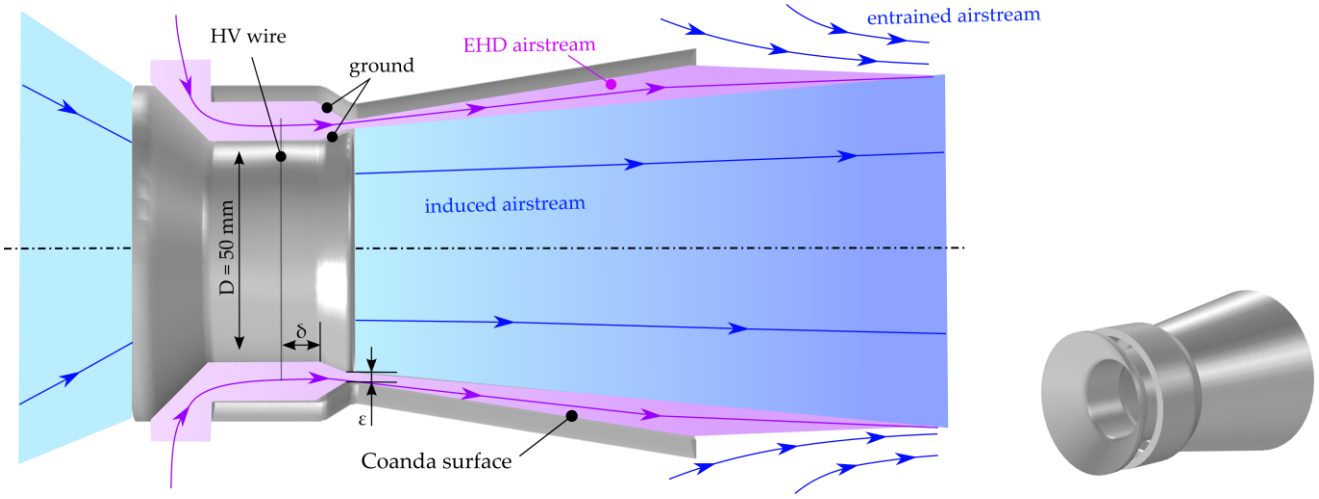

Figure 4: The open-space configuration of EHD air amplification is a 2D-axisymmetric geometry where the electrical components are embedded in the overlapping region of two separate pieces. Within the overlapping region the primary stream (EHD airstrem) is generated and pushed through the nozzle with gap size ε. As the EHD airstream remains attached to the Coanda surface it also induces an airstream in the inner volume. Due to the open space configuration, another airstream is accelerated, the entrained airstream, which further increases the flow rate.

2.4 Physics-based continuum model

In order to run the specified calculations, a fully coupled corona discharge- computational fluid dynamics (CFD) flow model is developed, which lowers the computational cost. Hence, three governing equations are calculated in a single study step. However, most single-species EHD numerical models, where the ionized fraction of air is described by the continuum variable space charge density, rely on a multi-step approach involving guessing the initial space charge on the emitting electrode [14]–[16]. Indeed, physics-based modeling of EHD is a complex endeavor due to the a priori unknown initial space charge generated on the corona discharge wire at a given voltage. This section discusses the governing equations used for the coupled EHD and airflow and proposes a novel approach to dynamically compute the initial space charge within the solver loop by adding a Lagrange multiplier as correcting variable.

2.4.1 Corona discharge model

The corona discharge part of the EHD model features Poisson's equation (Eq. (1)) with the electric potential ϕ [V] as the dependent variable, and the charge convection model with the space charge density ρ_{el} [C m^{-3}] as the dependent variable. The first governing equation writes

$$\nabla^2\phi = -\frac{\rho_{el}}{\varepsilon_0\varepsilon_r} \tag{1}$$

with ε_0 the vacuum permittivity (in air, $\varepsilon_r = 1$). The second governing equation is the conservation of charge, i.e., the continuity equation for current density, $\boldsymbol{J}$ [A m^{-2}],

$$\nabla \cdot \boldsymbol{J} = 0. \tag{2}$$

Conveniently, we can express the current density $\boldsymbol{J}$ in terms of Ohm's law and by defining the electric field as $\boldsymbol{E} = -\nabla\phi$

$$\boldsymbol{J} = \rho_{el} b\boldsymbol{E} + \rho_{el}\boldsymbol{u} - D_{ion}\nabla\rho_{el}. \tag{3}$$

Here, b stands for the ion mobility (in air, 1.8×10^{-4} m^2 V^{-1} s^{-1}), $\boldsymbol{u}$ [m s^{-1}] is external convection and D_{ion} [m^2 s^{-1}] is the ion diffusivity. Often, the diffusive ($D_{ion}\nabla\rho_{el}$) and external convection terms ($\rho_{el}\boldsymbol{u}$) are neglected due to the dominance of up to two orders of magnitude of the electrical field-based ion shift term in Equation (3) [1], [17]. Nevertheless, we also note that the diffusive term may prove useful to improve numerical stability. Furthermore, the electric field vector $\boldsymbol{E}$ can be expressed as the negative gradient of the electric potential. Hence, the corona discharge model is fully described by Equations (1) to (3) with two dependent variables, ϕ and ρ_{el}, requiring at least two boundary conditions for the electric potential and one boundary condition for the space charge density.

The boundary condition for the initial space charge requested by Equation (2) is of the Dirichlet-type and a priori unknown for single-species modeling approaches. While it is possible to find its value iteratively, it remains a tedious and time-consuming procedure that needs to be repeated for each electric potential value. Moreover, a single initial space charge value on the electrode can produce errors as the value is not necessarily constant over the entire boundary as detailed in Supplementary Material C. Employing a constant initial space charge density on the electrode is error-prone.

We avoid such numerical errors by retrieving the information for the initial space charge $\rho_{el,0}$ directly from Poisson's equation. Here, instead of specifying the given electric potential ϕ_1 on the wire, we enforce a weak constraint on the electrode boundary.

$$0 = (\phi_1 - \phi). \quad (4)$$

For practical implementation, equation (4) is defined by test functions or any other suitable optimization method. We chose the Lagrange multiplier approach, where the constraint is enforced by introducing another dependent variable, λ, within the solver loop. Conveniently, the newly introduced Lagrange multiplier variable is the initial space charge density $\lambda = \rho_{el,0}$, which can then be inserted into Equation (2). The boundary condition for the grounded electrode remains unchanged and is of Dirichlet-type, i.e. $\phi_1 = 0\,\mathrm{V}$.

The information about the electric field on the boundary is needed as well. We retrieve the information via an electric displacement boundary condition

$$\boldsymbol{D_0} = [0 \quad -\varepsilon_0 E_e]^{\mathrm{T}} \quad (5)$$

The electric displacement vector $\boldsymbol{D_0}$ is parallel to the normal boundary vector. E_e is the empirically defined electric field strength on the surface of the electrode

$$E_e = E_0 \left(1 + \frac{2.62 \times 10^{-2}}{\sqrt{r_e}}\right) \quad (6)$$

with $E_0 = 3.31 \times 10^6\ [\mathrm{V\,m^{-1}}]$ being the ionization breakdown electric field strength in air at standard conditions for a smooth electrode [18]. This is the generally accepted breakdown condition to invoke corona discharge, also known as the Peek-Kaptzov assumption [19]. With Equation (6), we complete the description of the fully automatized corona discharge modeling approach. The critical point of this coherent formulation is to replace the electric potential on the discharge electrode with a weak formulation of the electric potential and simultaneously include information about the required electric field on the same boundary. We need to match the electric potential weak constraint and the electric field condition. Thus, we introduce another fitting parameter as the Lagrange multiplier, which can then be deployed as the boundary condition for the initial space charge into the charge transport equation. This way, we enable the efficient calculation of extensive parametric studies, by avoiding the iterative determination of the space-charge density boundary condition.

2.4.2 Turbulent airflow computational fluid dynamics (CFD) model

The Navier-Stokes momentum equation describes the airflow part of EHD air amplification with an additional source term for the Coulomb force $\boldsymbol{F_c}$ **[N].**

$$\rho \boldsymbol{u} \cdot \nabla \boldsymbol{u} = -\nabla p + \mu \nabla^2 \boldsymbol{u} + \boldsymbol{F_c} \quad (7)$$

$$\boldsymbol{F_c} = \rho_{el} \boldsymbol{E}. \quad (8)$$

Here, ρ is the air density [kg m^{-3}], $\boldsymbol{u}$ is the velocity field [m s^{-1}], p is the pressure [Pa], and μ is the dynamic viscosity [Pa s]. Via the Coulomb force, the airflow model couples to the corona discharge model for the full EHD model.

We adopt a Reynolds-averaged Navier Stokes (RANS) approach in the airflow model. The standard $k-\varepsilon$ turbulence model is chosen to represent non-laminar behavior in CFD. This model is still the industrial standard [20]. Several other models were tested, e.g., $k-\omega$, SST, v2f with and without wall functions. In the studies, the mesh adjacent to walls was sufficiently refined in order to obtain values of about 1 for the dimensionless wall distance y^+. At such small y^+, the viscous sublayer of wall-bounded flows is resolved in a high confident level. We observed that the $k-\varepsilon$ turbulence model in combination with wall functions and a boundary layer mesh size respecting $y^+ \approx 1$ gives satisfactory accuracy in representing the Coanda effect in our configurations.

2.4.3 Boundary conditions

Figure 5 and **Error! Reference source not found.** summarize the necessary boundary conditions for EHD calculations with the above described Lagrange multiplier approach. Note that the boundary conditions are given for the constrained EHD air amplification configuration. For the benchmark case the conditions are the same except for the vane inlet that is not applicable, and the channel inlet becomes an inlet with total pressure $p_{tot} = 0\,\mathrm{Pa}$ instead of an opening. For the open space EHD air amplification configuration, the air domain is much larger and has an opening with 0 static pressure.

For EHD air amplification cases, the computational region consists of two domains, an air domain Ω_{air} and a polylactic acid (PLA) domain Ω_{PLA} with an assumed relative permittivity of $\varepsilon_r = 3$ [21]. PLA is chosen as the material for the enclosure due to its widespread use in additive manufacturing. An enclosure of such geometric complexity is ideally manufactured in a 3D-printed way to continue our research on EHD air amplification experimentally. Within the air domain, a density $\rho = 1.2\,\mathrm{kg\,m^{-3}}$, dynamic viscosity $\mu = 1.81 \cdot 10^{-5}\ \mathrm{Pa\,s^{-1}}$ and a relative permittivity of $\varepsilon_r = 1$ are assumed.

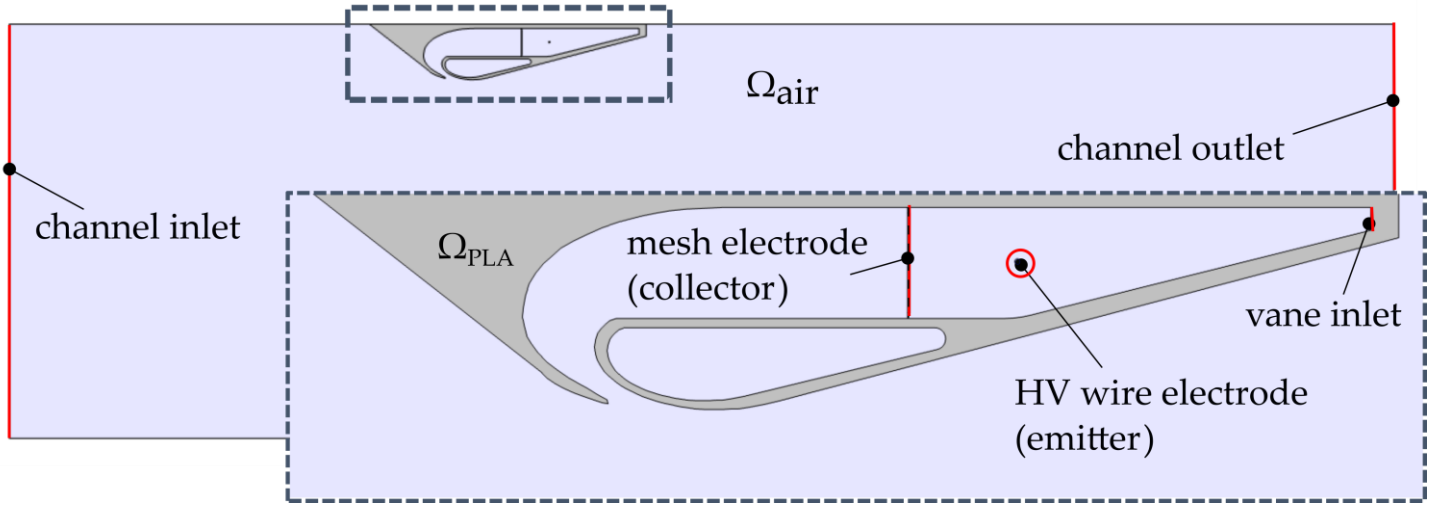

Figure 5: Configuration (a) with highlighted boundaries. The non-highlighted boundaries are no-slip walls.

Table 1 - Boundary conditions overview for configuration (a).

Boundary	Poisson Equation (1)	Charge Transport (2),(3)	Airflow (7)
Channel inlet	Zero charge	Zero flux	Opening, $p = 0$ Pa
Channel outlet	Zero charge	Zero flux	Opening, $p = 0$ Pa
Vane inlet	Zero charge	Zero flux	Inlet, $p_{tot} = 0$ Pa
Mesh electrode	$\phi = 0$ V	Zero flux	Wire mesh 30 % solidity (damping screen)
Wire electrode	$\boldsymbol{D_0} = [0 \quad -\varepsilon_0 E_0]^{\mathrm{T}}$ and $(\phi_1 - \phi) = 0$	$\rho_{el} = \rho_{el,0}$	No-slip wall
Elsewhere	Zero Charge	Zero flux	No-slip wall

2.5 Simulation runs

We explore the parameters in the design space of EHD air amplification with the confined space and open space EHD air amplification configurations while the regular EHD configuration serves as a reference point. Prior to the parametric studies, a validation case is run on a different geometry according to [18]. Additionally, a fluid flow-only case is calculated for the confined space configuration where a standard velocity inlet replaces EHD within the vane to test the aerodynamical operation range of the proposed geometry. The complete set of simulation runs with varying parameters is given in Table 2. The open-space simulation OSc_diameter is also a parametric study where only the inner diameter of the construction varies from 10 to 100 mm. In practice, a real EHD device with a gap of $\delta = 5$ mm and a voltage of $U_e = 30$ kV (e.g., CSa_deltaPhi) would likely produce an electrical arc. The arching effect is not modeled in these simulations.

Table 2 – Simulation list of computational configurations and parameter settings.

Name	Type	Description / Configuration	Wire radius r_e [µm]	Electrode spacing δ [mm]	Voltage ϕ_1 [kV]	Channel height H [mm]	Vane slit ε [mm]
CS0_validation	parametric	validation case [18], [19]	50	9	5-8	15	n/a
CSa_basecase	basecase	Confined space: amplifying	250	10	15	150	4
CSa_deltaPhi	parametric	Confined space: amplifying	250	5-25	10-30	150	4
CSa_wire	parametric	Confined space: amplifying	50-300	10	15	150	4
CSa_slit	parametric	Confined space: amplifying	250	10	15	150	1-10
CSa_height	parametric	Confined space: amplifying	250	10	15	50-150	4
CSa_onlyFlow	parametric	Confined space: amplifying	n/a	n/a	n/a	150	4
CSb_basecase	bascecase	Confined space: non-amplifying	250	10	15	150	n/a

CSb_deltaPhi	parametric	Confined space: non-amplifying	250	5-25	10-30	150	n/a
OSc_diameter	parametric	Open space: amplifying	50	10	30	n/a	4

2.6 Model implementation into numerical simulations

We implement the physics-based EHD model in COMSOL Multiphysics version 5.6, a commercially available finite element software. Corona discharge and airflow physics are solved in one fully coupled solver study. The COMSOL physics modules are "Electrostatics", "Coefficient Form PDE" and "Turbulent Flow, k − ε". The parameters are varied using parametric sweeps for the simulations in Table 2. The chosen solver is a fully-coupled direct solver, MUMPS (MUltifrontal Massively Parallel sparse direct Solver), combined with linear shape functions. For CFD, we adopt a PARDISO (PARallel Direct sparse SOlver) segregated solver with quadratic shape functions. For parametric studies, the solver was instructed to store NaN (Not-a-Number) solutions to track the feasibility of the design space parameter combinations. Moreover, the maximum number of iterations was set at 500 for each single sweep.

A mesh sensitivity analysis was performed on three separate grids (coarse, medium, fine) with 14 192, 28 029 and 56 050 elements. Via Richardson extrapolation, we found that the coarse mesh differs from the exact solution by a relative error of < 2 %. Hence, the simulations listed in Table 2 are performed on the coarse mesh. The computational grid is semi-automatically defined with the built-in mesher tool. It comprises mixed elements with strategic refinements in regions of interest or where steep gradients are expected, i.e., on the electrode boundary.

2.7 Metrics to evaluate the performance of EHD air amplifier

We evaluate the EHD air amplifier performance based on few metrics, namely the electric current, electric power, the airflow rates, and the flow to power ratio. The electric current I [A] is calculated directly via a boundary integral of the current density of the emitting wire

$$I = H \cdot \int_0^{2\pi r_e} \rho_{el} b \boldsymbol{E}\, ds \tag{9}$$

where H [m], being the height and depth of the 2D channel, adjusts the current per unit wire ds [m] to current over the entire wire with ds being oriented along the perimeter of the wire. Note that the integral is coordinate-adjusted for the open space configuration. The required electrical power is then straightforwardly obtained

$$P_{el} = I \cdot \phi_1 . \tag{10}$$

For the airflow rates $\dot{V}$ [$m^3\ s^{-1}$], we take the integral over the boundary, i.e., for the total flow rate, the integral over the channel outlet

$$\dot{V} = H \cdot \int_0^H \boldsymbol{u}\, dy \tag{11}$$

whereas for the average velocity $\bar{u}$ [$m\ s^{-1}$], the expression is

$$\bar{u} = \frac{1}{H} \int_0^H \boldsymbol{u}\, ds. \tag{12}$$

For the open space case, the flow-related integrals are taken 450 mm downstream from the electrode. Also, for the open space case the Equations (9)-(12) are formulated in terms of axisymmetric systems. Another important metric is the amplification factor, simply the ratio between EHD-generated and amplified airstream.

$$AF = \frac{\int_{Outlet} \boldsymbol{u}\, ds}{\int_{Inlet} \boldsymbol{u}\, ds}. \tag{13}$$

Lastly, as a measure of efficiency, we evaluate the flow to power ratio, i.e. the flow rate per electrical power γ [$m^3\ h^{-1}\ W^{-1}$],

$$\gamma = \frac{\dot{V}}{P_{el}}. \tag{14}$$

3 Results

3.1 Proof-of-concept constrained flow EHD air amplification

3.1.1 Air amplifier vane aerodynamic performance with and without EHD

The purpose of this section is to understand the aerodynamic performance of the vane as in **Error! Reference source not found.**, first without and then with EHD. We do this by showing the pressure-flow rate characteristic to assess which flow rates correspond to how much electrical power input. In Figure 6, the curve shows the performance of this particular geometry in standard settings. We obtain the vane air amplifier curve without EHD by simulating CFD-only mode with an imposed velocity inlet within the vane.

When operating the vane with EHD airflow generation, there is a maximal airflow rate that we can achieve for the current vane, as otherwise breakdown occurs. The shaded area shows values obtained from EHD air amplification simulations at the closest electrode distance $\delta = 5$ mm, since it provides the strongest flow rates, see also Figure 9b. Moreover, the electric power demand lines are plotted for a given flow rate. In the simulations, the highest achieved airflow rate is $\dot{V} = 407 \frac{\mathrm{m}^3}{\mathrm{h}}$ for the enclosed EHD air amplifier configuration. For such a flow rate, an electric power of 470 W is predicted by the simulations. In practice, this value is too high for corona discharge and instead of a continuous discharge, a spark would form. Sparks are highly non-linear phenomena that are not included in our model due to complexity reasons. We keep the high power prediction here for theoretical reasons. However, with another discharge principle, dielectric barrier discharge (DBD), higher power levels are achievable also in practice, but this is beyond the scope of this study.

An electrical power input for EHD airflow of 10 W is more realistic. It is clear that with 10 W, flow rates of less than 100 m^3/h with little supply pressure can be achieved. Hence, the chosen configuration for constrained flow EHD air amplification is probably preferred for high-pressure applications.

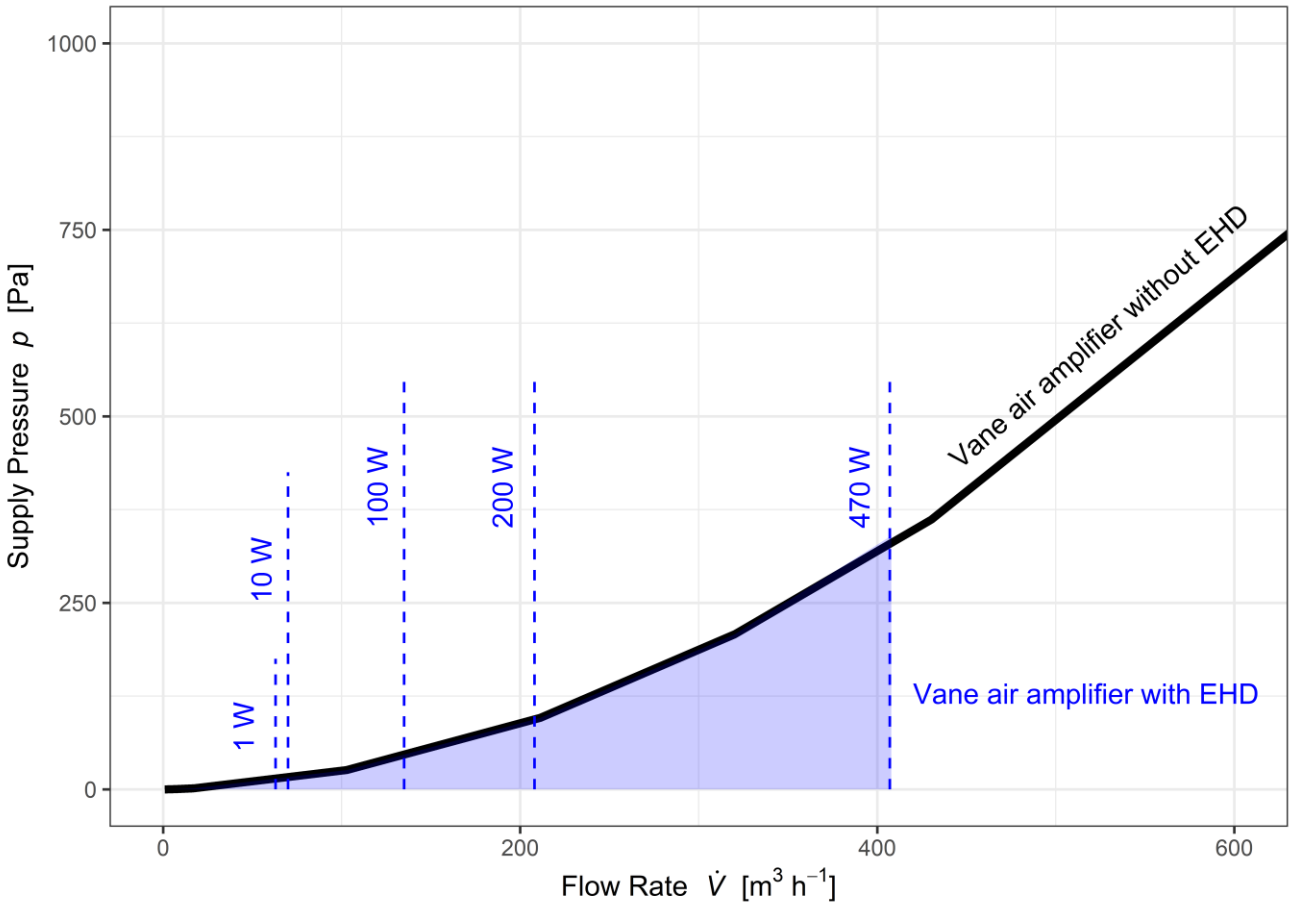

Figure 6: Supply pressure and flow rate characteristics of the configuration (a) vane enclosure. The supply pressure is the static fluid pressure within the vane while the flow rate is taken at the outlet of the 2D channel.

3.1.2 Impact of geometrical parameters on EHD air amplification performance

In this section we describe how geometrical parameters affect the air amplification performance of the EHD-equipped vane. The geometrical parameters are the size of the vane nozzle gap ε and the height of the channel H as flow confinement parameters of the EHD air amplification confined space configuration. Also, we include the radius of the electrode r_e as a geometrical parameter impacting both the fluid flow and electrical performance. We evaluate the volume flow rate at the end of the channel and efficiency in terms of flow rate per electrical power at the basecase voltage $\phi_1 = 15$ kV and an inter-electrode distance = 10 mm. Figure 7 summarizes the results for flow rate and efficiency under the influence of the described geometrical parameters. Note that the dashed line represents each parameter's arbitrarily chosen basecase value.

The most prominent finding is that there appears to be an optimum for the nozzle gap at $\varepsilon = 6$ mm. We obtain both maximum efficiency and volume flow rate, as seen in Figure 7a and Figure 7d. A too-large nozzle gap ($\varepsilon = 10$ mm) creates a flow separation zone that leads to flow detachment and that impedes the formation of the Coanda effect. The flow detachment is also shown in Figure 8b. A too-narrow gap ($\varepsilon = 1$ mm) seems to pose an important flow resistance that weakens the EHD-generated airstream and ultimately weakens the more significant, amplified bulk flow within the channel. According to Figure 7c and Figure 7f, we observe the flow rates rise with the larger size of the flow confinement area when it comes to the impact of the channel height. With increasing channel size the air entrainment has a more significant effect due to the larger volume of air available. The same

applies to the electrical power invested, which remains constant, and therefore more flow contributes to an overall efficiency gain. The results indicate an opposite behavior in maxima and minima for the wire radius. The volume flow rate is at its maximum for the smallest dimension, r_e = 50 µm, as seen in Figure 7b. This is due to the stronger curvature of the wire, which yields a stronger electric field and thus a more potent Coulomb force which translates into an increase in momentum transfer. Conversely, the efficiency curve in Figure 7e demonstrates that larger wire diameters are beneficial for obtaining more flow for the same electrical power input. The wire radius poses a design challenge where a trade-off must be found.

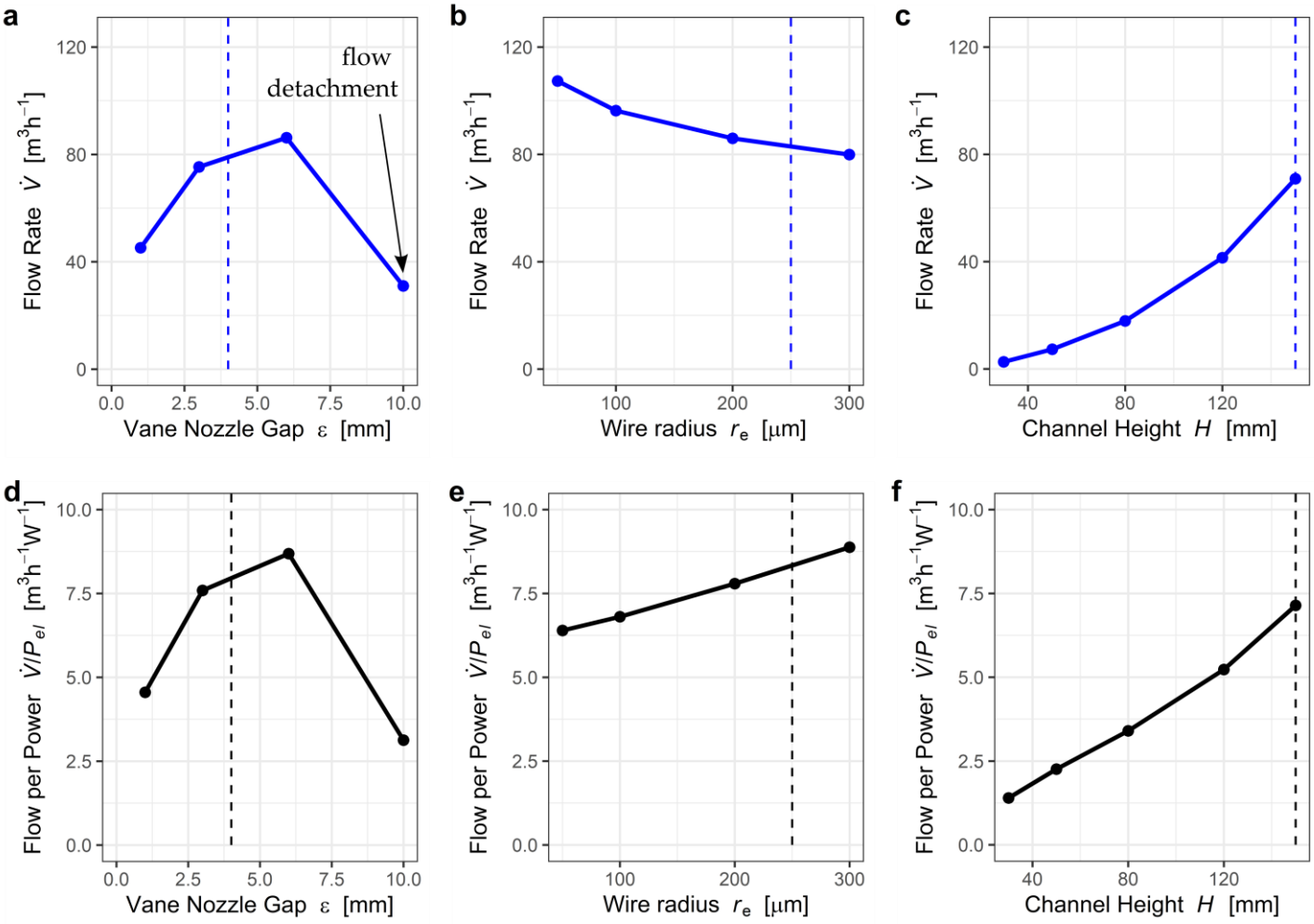

Figure 7: Flow rate and efficiency results for various geometrical parameters. (a) to (c) show the behavior of the channel bulk flow rate under the influence of vane nozzle gap, wire radius, and channel height. The graphs (d) to (f) show the impact on efficiency. The dashed lines represent the standard base case settings for each corresponding parameter setting.

In Figure 8, flow fields and the space charge density field are shown for selected cases. The results depicted in Figure 8a, and Figure 8c correspond to the optimum for the nozzle gap size ε = 6 mm where efficiency and volume flow rate are expected to be highest. For this parameter selection, EHD air amplification operates as intended. The EHD-generated airstream remains attached to the Coanda surface of the vane enclosure and drags the air within the channel along.

In the following picture, Figure 8b, we see a non-operational EHD air amplifier, which happens if the gap size is too large, i.e., ε = 10 mm and above. Figure 8b also explains the substantial decay in volume flow rate and efficiency, as seen in Figure 7a and Figure 7d. Note that the gap size is too large for this configuration. The in-vane flow takes a 180-degree turn and, with a 10 mm gap, will just shoot to the bottom of the channel, without attachment of the air jet due to the Coanda effect. It is indeed possible to create a geometry where the Coanda effect and flow attachment persists even with a gap size of ε = 10 mm or more. Such a geometry would for example be a nozzle that ends on a flat plate. So for this convex surface, there is an optimum gap size. However, the concept of EHD air amplification is strongly geometry-dependent such that a general answer on the ideal nozzle size cannot be given.

Figure 8d depicts the space charge density distribution, and it looks similar for all parameter variations of electric potential, vane nozzle gap size, and wire radius. What changes is mostly the intensity of the space charge density. We show the ionized, electrically conductive part of air with the space charge density distribution. It also represents the area where the Coulomb force acts on the air. The acceleration region can be seen, i.e., also in the velocity field in Figure 8c. There is the inter-electrode space where the airflow experiences a strong acceleration. In fact, by integrating the electrodes within an enclosure such as a vane, in this case, practical applications can be targeted. In practice, high voltage components need to be shielded from the surroundings for safety

reasons. Our simulations also show no more electrical charges downstream the mesh ground, which means that we can assume the channel bulk flow to be charge-free. Charge-free flow is another advantage EHD air amplification has over regular EHD when safety issues are of concern.

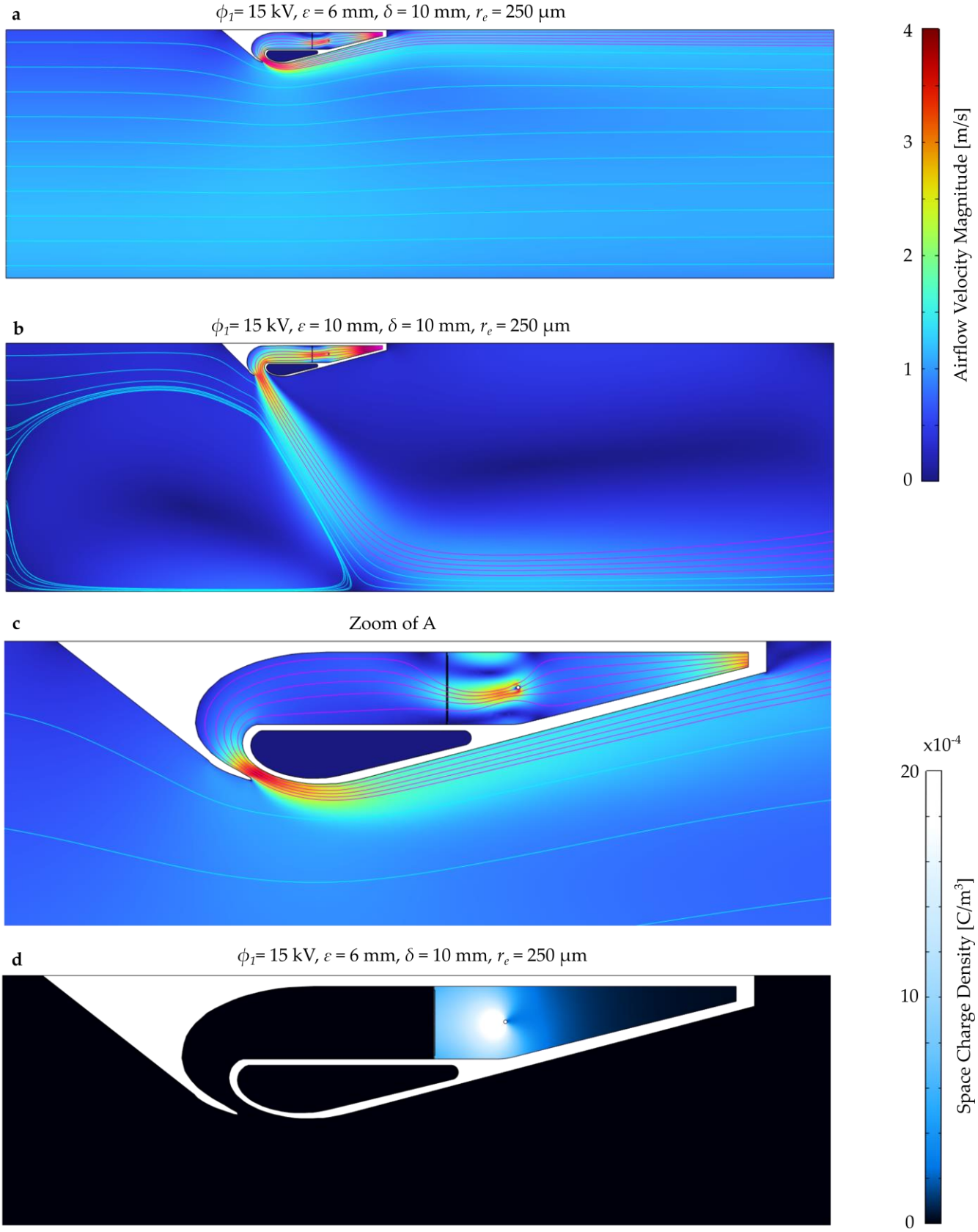

Figure 8: Selected EHD air amplifier flow fields for the flow field (a) to (c) and space charge density distribution (d). The EHD-generated flow is marked by magenta streamlines while the amplified flow rate is cyan. Subfigure (a) and (b) differ in nozzle gap size, exemplarily showing that the flow detaches from the Coanda surface in the latter case.

3.1.3 Electrical and flow performance maps of regular EHD and EHD air amplification

As a result of the parametric studies of the configurations for EHD air amplification ("amplifying") and regular EHD ("non-amplifying") we show the performance maps in Figure 9. The amplifying configuration features the vane enclosure where the electric potential varies from 10 to 30 kV. Also, the electrode distance is varied between 5 to 25 mm. The same parametric study is duplicated for the regular EHD case without air amplification. One of the most important result is the voltage-current relationship, as per Figure 9a. Here, both configurations show similar behavior, with about 20 % higher current on behalf of the amplifying case, which means that the vane enclosure animates the wire to produce more charge. Note that the distance of the electrode has an essential impact on the corona discharge onset voltage. While at the smallest distance, $\delta = 5$ mm, we can produce EHD-flow at $\phi_1 = 10$ kV already, the onset for 25 mm distance occurs after 16 kV. In Figure 9b, it shows the volume flow rate at the channel's outlet at various voltage levels. For the amplifying geometry, the flow rate encompasses the EHD-generated airstream plus the amplified airstream, while for the non-amplifying configuration, the flow chart is the EHD-generated airstream alone. The fields do not overlap. The non-amplifying case can provide higher flow rates up to more than 1000 $m^3\ h^{-1}$ over the entire voltage operation range. Also, we can see that a closer electrode distance generates more substantial airflow rates.

So far, the non-amplifying benchmark case outperforms the EHD air amplification configuration in terms of lower electric current consumption and higher flow rate. However, after a specific voltage, $\phi_1 \sim 16$ kV, the EHD air amplifier configuration shows superior efficiency as seen in the flow rate per electrical power chart in Figure 9c. For non-amplifying regular EHD, there is no electrode distance-dependent efficiency difference. Moreover, at lower voltages, the non-amplifying case is up to three times more efficient in generating a specific flow rate than the amplifying case. Afterward, the efficiency rapidly decreases, and the EHD air amplification becomes more performant, given that the electrodes are distant enough. For close distance, $\delta = 5$ mm, regular EHD still prevails in efficiency. For comparison, the red dashed line represents an ordinary compact DC axial fan of comparable size (Model 5318 /2 TDHHP, 66 W, 490 $m^3\ h^{-1}$, ebm-papst St. Georgen GmbH & Co. KG). In the domain of airflow generation, EHD air amplification appears competitive energy-wise with an increase in airflow generation efficiency of 34 to 48 % (at 10 to 19 kV) compared to this selected regular fan.

The flow rate per electric power is calculated from flow rate and electric current. The latter experiences a non-linear behavior that leads to a plateauing at increased voltage levels. This is evidence that increasing the total charge volume in the drift region affects the Coulomb force so the model momentum transfer to the air suffers in efficiency.

Another metric for airflow generation efficiency is the amplification factor. The invested electric energy is as a result of this locked within the EHD-generated airstream equivalent to a flow rate of $\dot{V}_{in}$ used for the Coanda effect. With this effect, a more significant bulk flow is induced with a flow rate $\dot{V}_{out}$. Figure 9d shows the performance map of the amplification factor. The amplification factor ranges from 16.5 to 19, the relative amount of airflow obtained is "for free" without costing further electrical energy. In comparison, air amplifiers typically amplify the incoming airstream up to a factor of 15 [22][23]. With the present EHD air amplifier numerical proof-of-concept in this work, a similar or even superior amplification factor completely bladeless can be achieved in a solid-state fashion.

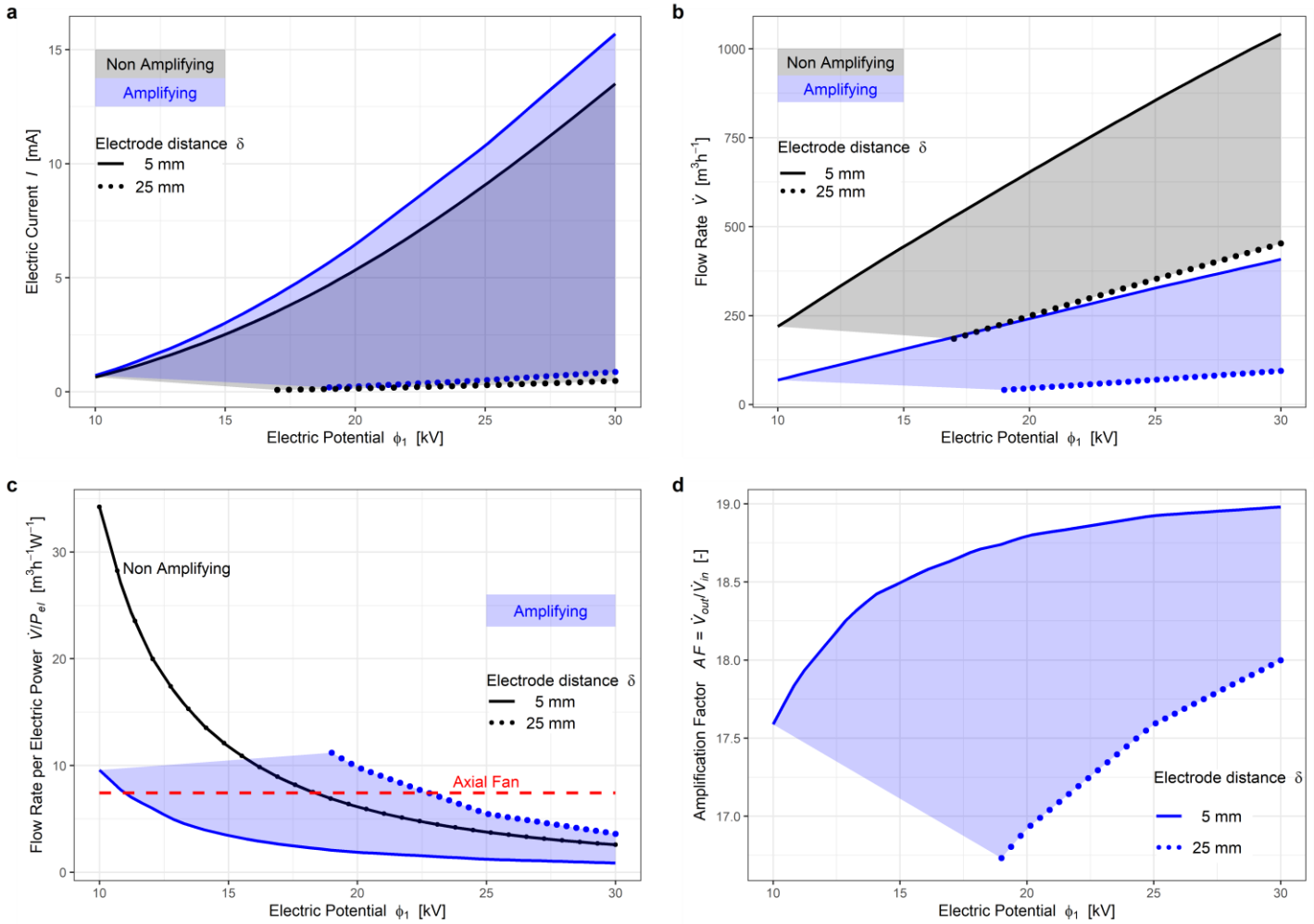

Figure 9: Electrical and flow performance maps resulting from parametric studies of the amplifying and non-amplifying (benchmark) configuration. Subfigures (a) and (b) directly compare the voltage-current relationship and the voltage-volume flow rate relationship. Subfigure (c) shows the flow rate to electric power ratio, including an ordinary axial fan, and (d) plots the amplification factor range.

3.2 Proof-of-concept open space EHD air amplification

3.2.1 Flow patterns of open space EHD air amplifiers

The open space EHD air amplifier construction consists of two independent components that overlap and form an enclosure. Inside, we accommodate the wire electrode and the ground electrode, embedded in both components' nozzle sections. In practice, the ground could be done via copper tape while the two PLA components are 3D-printed. Note that in this EHD air amplifier design, we have a non-convex straight Coanda surface with an angle of 9.26°. The shape and dimensions of the vane are arbitrarily chosen and will be studied in more detail in future research. Here, we show that EHD air amplification also works in open spaces for various dimensions. Many air amplifiers are used in the free field. As a reminder, to achieve EHD air amplification, three elements are necessary, a high voltage electrode (wire, needle, or any other shape with sub-millimeter curvature), an air cavity where the electrodes are embedded inside, and a Coanda surface, i.e. a surface facilitating the Coanda effect with subsequent air entrainment.

Those three necessary elements are built into this open space EHD air amplifier. In Figure 10a-d, there are cutouts of the larger flow field for different inner dimensions D while the other dimensions of the vane are kept constant. The EHD air amplifier takes surrounding air and forms an airstream jet. Downstream the airflow jet is where the total flow rate is measured. The total flow rate in open space consists of three connected airstreams: the EHD-generated airstream, the amplified airstream, and the entrained airstream. The latter is a collateral airstream dragged along the amplified airflow jet in the open space. We observe the entrained airstream in the plots as surrounding streamlines from the broader open space appear and accelerate in the propagation direction of the jet. Additionally, it is also noted that the size of the air amplifier has an impact on the evolution of the velocity between the inner Coanda surfaces. Smaller dimensions such as 10 and 20 mm, as per Figure 10a and Figure 10b, are forming a type of recirculation zone, and ultimately leading to an efficiency loss. Hence, the first results show that scalability is given. However, on a geometrical level, there is still space for streamlining for example by changing the angle of the Coanda surfaces or even curving them to form a convex shape.

Figure 10e shows the distribution of space charge density within the enclosure, which is similar as all cases. In the confined space EHD air amplifier case, it was observed that the space charge does not penetrate the larger bulk flow. The same situation is also given in this 2D-axisymmetric design, where the grounded electrode is embedded into the nozzle. We must also acknowledge that it is a special air amplifier design. In reality, the air supply is not so close to the entrainment area.

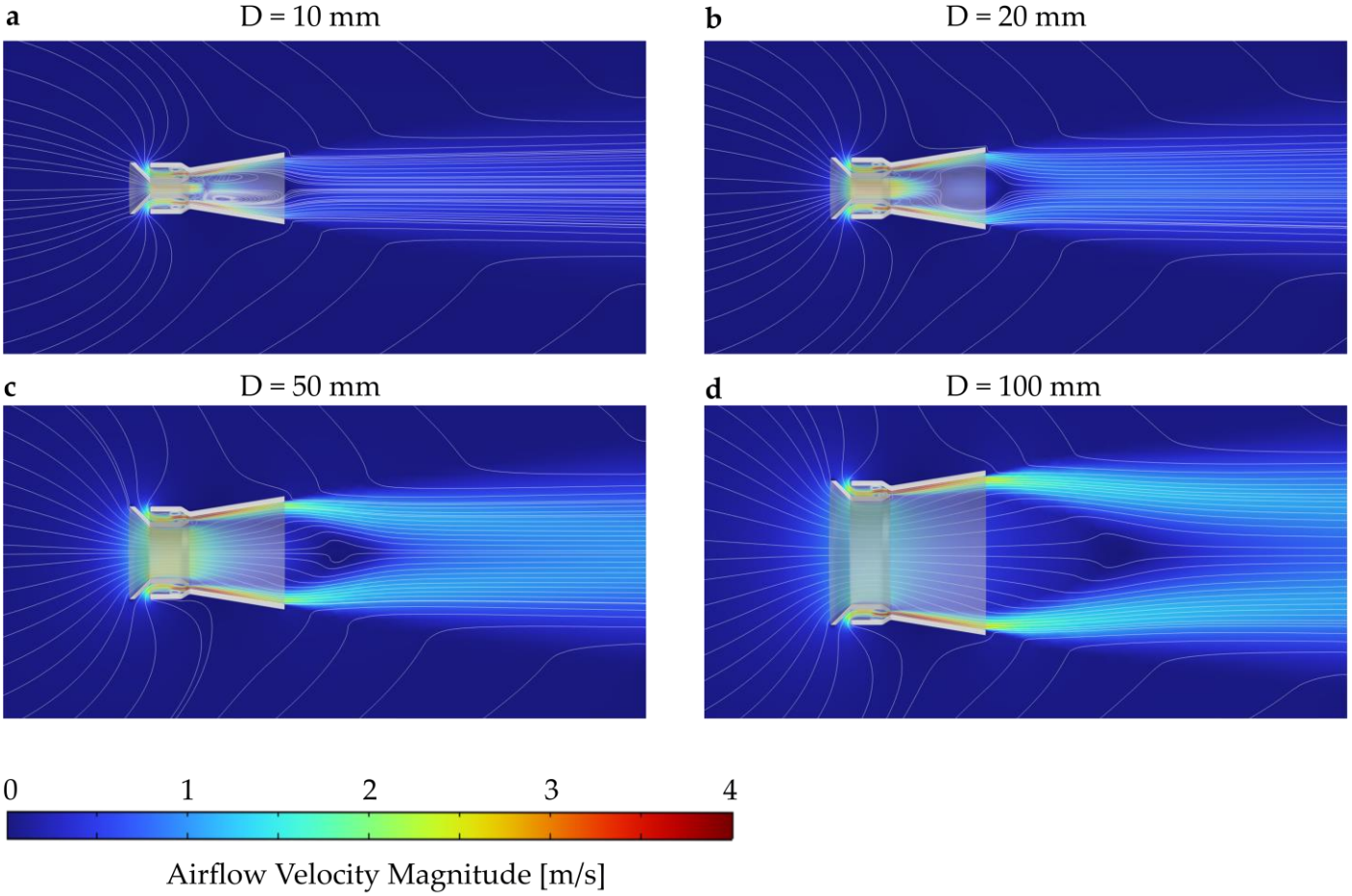

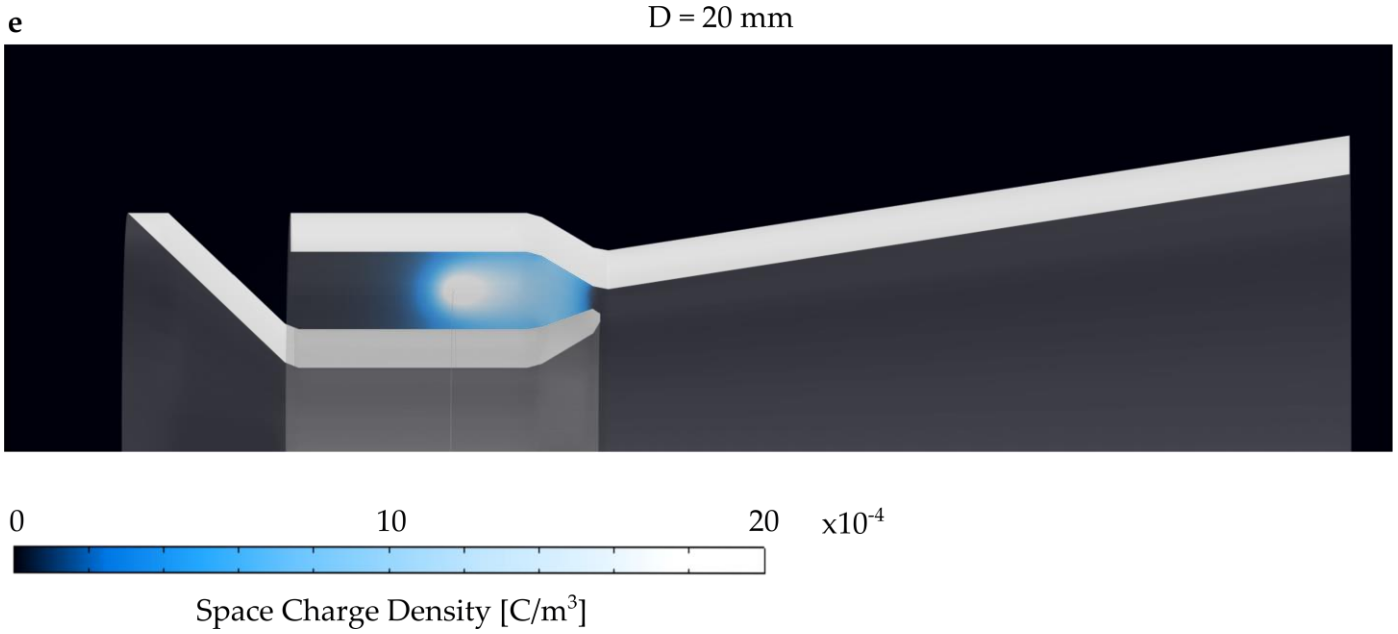

Figure 10: Velocity fields for the 2D-axisymmetric case configuration (c). The various inner diameter dimensions are portrayed by subfigures a-d. Subfigure E shows the space charge density distribution within the amplifying vane. In

contrast to confined flow EHD air amplification, the open space configuration also shows that surrounding air is dragged additionally via entrainment.

3.2.2 Impact of EHD air amplifier scaling on performance characteristics

Amidst the many parameters that can be checked in EHD air amplification, for the open space case, we will focus on the inner diameter of the device only as here we have the advantage of checking for scalability of the entrainment area of EHD air amplifiers. The goal is to achieve maximum flow rates. Hence the wire is set to $r_e = 50$ µm based on the findings shown in Figure 7b. The inter-electrode distance and gap size are kept as in the basecase simulation. The confined space EHD air amplifier vane and this discussed vane are only limitedly comparable for the electrode arrangement as the grounded electrode here is embedded within the nozzle. Also, the EHD-generated airstream does not reverse within the vane. Instead, it deviates up to a maximum clockwise angle of 90°. Hence, based on the previous calculations, only the information about the wire electrode radius is taken as a design parameter to achieve maximum flow rates.

The results for the electrical and flow performance are shown in Figure 11. With increasing inner diameter D from 10 to 100 mm, the circumference of the entire structure increases with it. The power consumption increases linearly, as seen in Figure 11a. The volume flow rate exhibits similar behavior as per Figure 11b, where the volume flow rate is measured at a distance of 350 mm from the vane. However, in terms of efficiency, there appears to be an optimum of as per Figure 11c. Here, an inner diameter of 50 mm performs about 10 % better than the smallest case with an inner diameter of 10 mm. Compared to the aforementioned axial fan, this open space EHD air amplifier provides more flow rates per electrical power invested over the entire range of sizes. Also, the chosen benchmark axial fan has dimensions of 140 x 140 mm (Model 5318 /2 TDHHP, 66 W, 490 $m^3\ h^{-1}$, ebm-papst St. Georgen GmbH & Co. KG). A solid-state and noiseless EHD air amplifier for downsized energy-efficient applications might be a worthwhile alternative to consider. Of course, in terms of flow rates, the axial fan still outperforms the EHD air amplifier by a factor of approximately 3.5 (when compared to the $D = 100$ mm setup). As further efficiency measure, we evaluate the amplification factor in Figure 11c. The amplification factor is somewhat difficult to determine in an open space environment as the EHD-generated airstream is part of the larger volume before entering the amplifier. However, in the established numerical simulations, the EHD-generated airstream $\dot{V}_{in}$ inside the vane can conveniently be retrieved by integration of the airflow velocity in that specific area. The results show that in open space, a considerably lower amplification factor up to 6.4 is obtained than the constrained EHD air amplifier, which was up to 19.

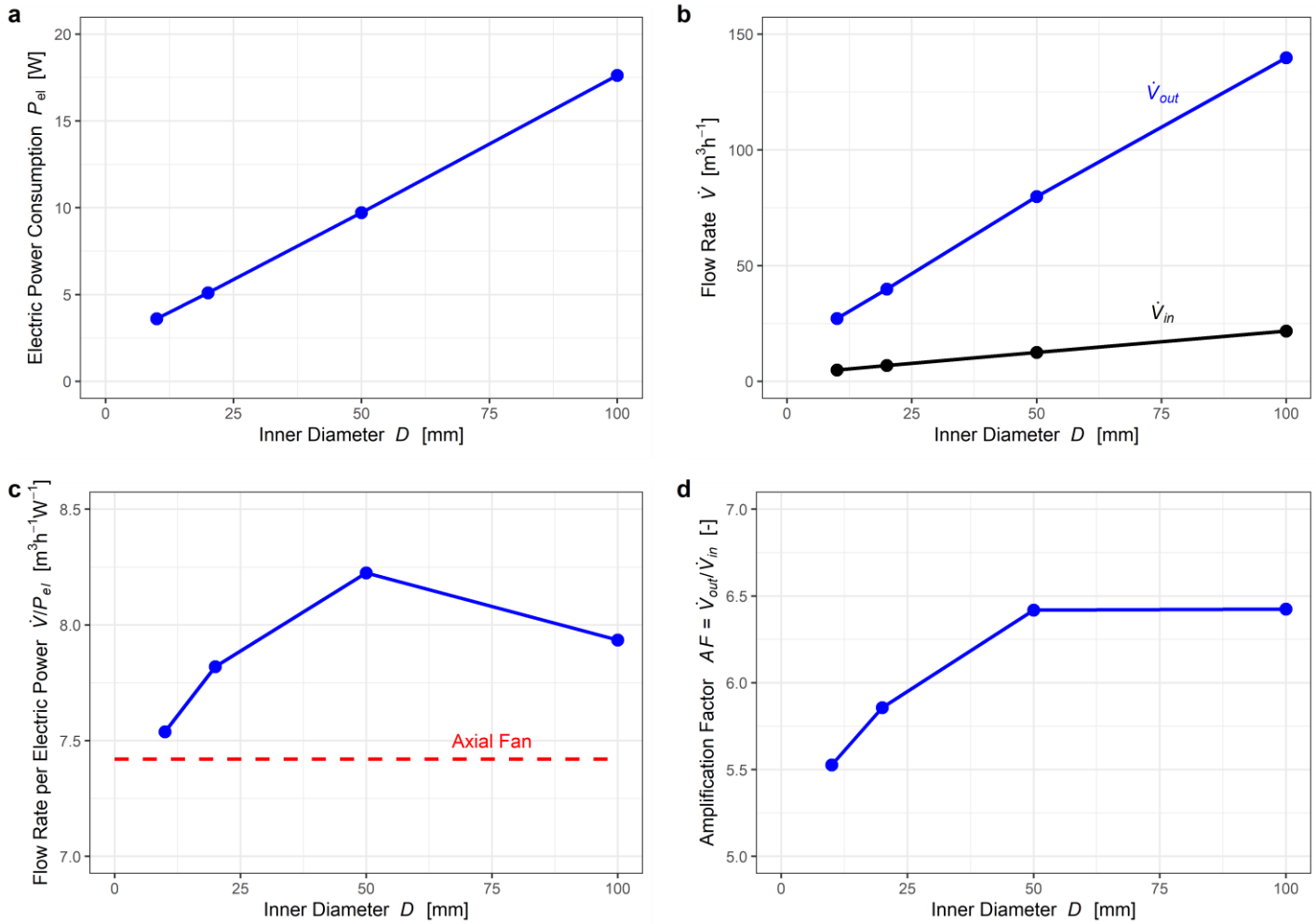

Figure 11: Electrical, flow, and efficiency results for the 2D-axisymmetric vane configuration (c) for various inner diameter dimensions. For comparison purposes, the efficiency in terms of flow rate per electric power also shows an ordinary axial fan.

4 Discussion

4.1 Numerical proof-of-concept of EHD air amplification

We demonstrated numerically the concept of a novel EHD air amplifier with the ambition to increase flow rates and to improve the notoriously low conversion efficiency from electrical to mechanical energy. The efficiency problem is inherent with EHD. The key novelty is to combine EHD with the Coanda effect, which allows using the EHD-airstream as a bleed flow to induce a larger bulk flow, thus boostering the flow rate and overall efficiency.

The vast design space of EHD air amplification is best explored with our fully-automated corona discharge numerical model. The numerical approach has been validated with experimental data [18] and also analytically verified in a test-case simulation. We studied two types of air amplifiers with this tool: a confined space configuration and an open space configuration. The confined space configuration has undergone extensive parametric runs. The goal of improving energy efficiency has been met. Compared to regular EHD and a commercial axial fan, the conceptual EHD air amplification is able to generate more flow rates per electrical energy invested after a threshold voltage of 19 kV. The regular EHD benchmark still produces higher flow rates in the confined channel setup, albeit at higher electrical costs. For the open space case, the second configuration shows that scalability is possible. Among the numerous study parameters, the geometry relevant ones play more significant role.

4.2 Potential applications of EHD air amplification

EHD air amplification is a potential candidate for various ventilation applications, both in industry and for domestic use. With the housing or enclosure an EHD air amplifier needs, we can separate the delicate high voltage components from the surroundings. We expect EHD air amplification technology to be adopted in in could, e.g., in

- Alternative devices
  - Noiseless fans
  - Ionic pumps

    - Solid-state, bladeless fans without moving parts
- Applications
    - Cooling
    - Active flow control
    - Surface drying
    - Extraction of gases and small particles
    - Decontamination / disinfection control

Disinfection control might be attractive to medical and food processing purposes as EHD air amplifiers produce ozone as a co-product. For domestic use, an EHD air amplifier must also remove or dilute the ozone to a sub-critical level. Ozone generation will be targeted in future studies. As such, EHD air amplifiers could serve, apart from airflow generation, also a decontamination function and even help in particle removal.

4.3 Possible hurdles and limitations in practical implementation

Several aspects might pose problems when translating the numerical study into an experimental prototype. EHD air amplification with a wire was systematically assessed on numerical level, and the numerical model could produce data for a wide operation range. However, in practice, such high voltages might result in sparkover, i.e., when the corona discharge is not continuous anymore and starts arching. The arching problem is also more present for wires in the presence of a dielectric such as the PLA enclosure since it has a higher permittivity or in environments with elevated humidity. A higher permittivity might distort the electric field in a way that makes it more homogeneous around the discharging electrode, and as such, the high gradients to sustain a continuous discharge are absent. Therefore, it is worth considering needle shapes or other sharply edged geometries as discharging electrodes for practical application.

Also note that EHD air amplifiers deliver a lower pressure by corona discharge and its resulting Coulomb force, compared to other commercially available air amplifiers. We generate a pressure lift of a few Pascal, whereas commercially available air amplifiers use a source of high-pressure air of more than 100000 Pa to operate and establish the Coanda effect.

Lastly, in particular parameter combinations, namely, when the voltage is high and the inter-electrode is close, several hundred Watt of electrical power are obtained, meaning a great potential leading much higher flow rate. In practice, EHD operates at a few Watt electrical power. Although such a strong power can be realized in silico, there is a serious risk of arching in practice.

5 Conclusion

This in-silico investigation dealt with modeling a novel type of low-energy airflow propulsion device, the so-called EHD air amplifier. Two configurations of EHD air amplifiers have been designed, one for confined space and one for open space. Another regular EHD configuration seved as benchmark. Several design space parameters have been explored with a Lagrange-multiplier modeling approach that allows fast and automatic calculation of single-species EHD-driven flows. We obtained extensive parametric results such as the volume flow rate, current-voltage relationships, efficiency in terms of flow rate per power, and amplification factors for both configurations. The key findings are:

- The EHD air amplifier in constrained flow configuration improves the energy efficiency at a voltage of 19 kV from 6.87 to 10.98 ($m^3\ h^{-1}$)/W (+59%). It remains more efficient than regular EHD also at higher operational voltages. Compared to a similar-sized axial fan, the EHD air amplifier yields a maximum efficiency increase of 48 %. Hence, EHD air amplifiers produce flow rates more efficiently per Watt invested than regular EHD devices and axial fans.
- In the constrained configuration, amplification factors of 16.5 to 19 are achieved. For the open space configuration, the amplification factor ranges from 5.5 to 6.4. EHD air amplifiers achieve similar amplification factors than normal air amplifiers.
- The open space configuration performs best energy-wise with an inner diameter of 50 mm, where the peak efficiency of 8.24 ($m^3\ h^{-1}$)/W is predicted. In terms of maximum flow rates, an inner diameter of 100 mm yields 137 $m^3\ h^{-1}$. The product is scalable and there is a sweet spot efficiency-wise

The obtained physics-based simulation study demonstrates that the high potential EHD air amplification can improve ionic wind's intrinsically inefficient generation of airflow rates. By air amplification, we can increase the airflow rates of EHD with a factor 19 in contrained flow and with a factor 6.4 in open space. Also, the model developed in this study allows for fast computation of EHD-driven flows, which gives valuable insight into the design of EHD air amplifiers and EHD technology in general. A wide range of domestic and medical applications can be targeted as potential use cases.

Acknowledgments

The authors are grateful to the Swiss Innovation Agency (Innosuisse 34549.1 IP-LS) for the financial support provided during project conceptualization and execution. This manuscript has been released as a preprint on engrXiv.

AUTHOR CONTRIBUTIONS

Donato Rubinetti: Conceptualization, Methodology, Investigation, Project Management, Writing – review, and editing. Kamran Iranshahi: Methodology, Writing – review, and editing. Daniel Onwude: Writing – review, and editing. Lei Xie: Methodology, Writing – review, and editing. Bart Nicolaï: Writing – review, and editing. Thijs Defraeye: Conceptualization, Methodology, Supervision, Funding Procurement, Project Management, Writing – review, and editing.

REFERENCES

[1] K. Iranshahi, A. Martynenko, and T. Defraeye, "Cutting-down the energy consumption of electrohydrodynamic drying by optimizing mesh collector electrode," *Energy*, vol. 208, p. 118168, Oct. 2020, doi: 10.1016/j.energy.2020.118168.

[2] M. Robinson, "Movement of air in the electric wind of the corona discharge," *Trans. Am. Inst. Electr. Eng. Part I Commun. Electron.*, vol. 80, no. 2, pp. 143–150, 2013, doi: 10.1109/tce.1961.6373091.

[3] R. Tirumala and D. B. Go, "Multi-electrode assisted corona discharge for electrohydrodynamic flow generation in narrow channels," *IEEE Trans. Dielectr. Electr. Insul.*, vol. 18, no. 6, pp. 1854–1863, Dec. 2011, doi: 10.1109/TDEI.2011.6118623.

[4] M. J. Johnson, R. Tirumala, and D. B. Go, "Analysis of geometric scaling of miniature, multi-electrode assisted corona discharges for ionic wind generation," *J. Electrostat.*, vol. 74, pp. 8–14, Apr. 2015, doi: 10.1016/J.ELSTAT.2014.12.001.

[5] Y. Wu *et al.*, "Greener corona discharge for enhanced wind generation with a simple dip-coated carbon nanotube decoration," *J. Phys. D. Appl. Phys.*, vol. 50, no. 39, p. 395304, Sep. 2017, doi: 10.1088/1361-6463/AA81A9.

[6] S. Kanazawa, W. Imagawa, S. Matsunari, S. Akamine, R. Ichiki, and K. Kanazawa, "Ionic Wind Devices Prepared by a 3D Printer." Accessed: Oct. 14, 2021. [Online]. Available: https://ijpest.securesite.jp/Contents/11/1/PDF/11-01-038.pdf.

[7] M. Rickard, D. Dunn-Rankin, F. Weinberg, and F. Carleton, "Maximizing ion-driven gas flows," *J. Electrostat.*, vol. 64, no. 6, pp. 368–376, Jun. 2006, doi: 10.1016/j.elstat.2005.09.005.

[8] G.-W. Zhang and J.-K. Yang, "A review on recent advances and challenges of ionic wind produced by corona discharges with practical applications You may also like Numerical simulation on ionic wind in circular channels," *J. Phys. D Appl. Phys. Top. Rev.*, vol. 55, p. 153002, 2021, doi: 10.1088/1361-6463/ac3e2c.

[9] J. Wang, Y. jun Liu, T. Zhu, Y. qiang Chen, and J. bo Wang, "Magnetic field enhanced ionic wind for environment-friendly improvement and thermal management application," *Appl. Therm. Eng.*, vol. 194, p. 117054, Jul. 2021, doi: 10.1016/j.applthermaleng.2021.117054.

[10] D. Zhou, J. Tang, P. Kang, L. Wei, and C. Zhang, "Effects of magnetic field intensity on ionic wind characteristics," *J. Electrostat.*, vol. 96, pp. 99–103, Dec. 2018, doi: 10.1016/J.ELSTAT.2018.10.007.

[11] T. Panitz and D. T. Wasan, "Flow attachment to solid surfaces: The Coanda effect," *AIChE J.*, vol. 18, no. 1, pp. 51–57, Jan. 1972, doi: 10.1002/aic.690180111.

[12] A. Dumitrache, F. Frunzulica, and T. C. Ionescu, "Mathematical Modelling and Numerical Investigations on the Coanda Effect," in *Nonlinearity, Bifurcation and Chaos - Theory and Applications*, InTech, 2012.

[13] P. D. Gammack, F. Nicolas, and K. J. Simmonds, "FAN," US 8,308,445 B2, 2012.

[14] A. Kasdi, "Experimental and numerical modeling of corona discharge generated in an electrostatic precipitator," Jan. 2019, doi: 10.1109/CISTEM.2018.8613435.

[15] T. Defraeye and A. Martynenko, "Electrohydrodynamic drying of food: New insights from conjugate modeling," *J. Clean. Prod.*, vol. 198, pp. 269–284, 2018, doi: 10.1016/j.jclepro.2018.06.250.

[16] D. I. Onwude, K. Iranshahi, D. Rubinetti, A. Martynenko, and T. Defraeye, "Scaling-up electrohydrodynamic drying for energy-efficient food drying via physics-based simulations," *J. Clean. Prod.*, vol. 329, p. 129690, Dec. 2021, doi: 10.1016/J.JCLEPRO.2021.129690.

[17] Y. Guan, R. S. Vaddi, A. Aliseda, and I. Novosselov, "Analytical model of electro-hydrodynamic flow in corona discharge," *Phys. Plasmas*, vol. 25, no. 8, Aug. 2018, doi: 10.1063/1.5029403.

[18] N. E. Jewell-Larsen, S. V Karpov, I. A. Krichtafovitch, V. Jayanty, C.-P. Hsu, and A. V Mamishev, "Modeling of corona-induced electrohydrodynamic flow with COMSOL multiphysics," *Proc. ESA Annu. Meet. Electrost.*, pp. 1–13, 2008.

[19] A. A. Ramadhan, N. Kapur, J. L. Summers, and H. M. Thompson, "Numerical modelling of electrohydrodynamic airflow induced in a wire-to-grid channel," *J. Electrostat.*, vol. 87, pp. 123–139, Jun. 2017, doi: 10.1016/j.elstat.2017.04.004.

[20] T. Defraeye and A. Martynenko, "Electrohydrodynamic drying of food: New insights from conjugate modeling," *J. Clean. Prod.*, vol. 198, pp. 269–284, Oct. 2018, doi: 10.1016/j.jclepro.2018.06.250.

[21] B. Behzadnezhad, B. D. Collick, N. Behdad, and A. B. McMillan, "Dielectric Properties of 3D-Printed Materials for Anatomy Specific 3D-Printed MRI coils," *J. Magn. Reson.*, vol. 289, p. 113, Apr. 2018, doi: 10.1016/J.JMR.2018.02.013.

[22] L. C. Mansson and S. H. Traberg-Larsen, "Flow Characteristics of the Dyson Air Multiplier," *Comput. Fluid Dyn. using Ansys Fluent*, vol. 14.5.7, pp. 1–7, 2014.

[23] "Air Technology Air Efficiency Range," Accessed: Nov. 10, 2021. [Online]. Available: www.meech.com.

[24] D. Rubinetti, D. A. Weiss, and W. Egli, "Electrostatic Precipitators-Modelling and Analytical Verification Concept," *2015 COMSOL Conf. Grenoble*, pp. 14–16, 2015, [Online]. Available: https://www.comsol.com/paper/download/291561/rubinetti_paper.pdf/%0Ahttps://www.comsol.com/paper/electrostatic-precipitators-modeling-and-analytical-verification-concept-25951.

SUPPLEMENTARY MATERIAL

A Validation of the EHD model with experimental data

To prove the validity of our modeling approach as described in Section **Error! Reference source not found.**, we adopt it on a set of experimental data, which also includes a simulation model from Jewell [18]. The settings and geometry is exactly as outlined in the reference. The only modification is the boundary condition on the emitter electrode, where we adopted the Lagrange Multiplier approach as in Section 2.4.1 and 2.4.3.

Our results show good agreement with experimental data, as seen in Figure 12. We obtain an overprediction of electric current at an electrode voltage of 8 kV while the remaining data points match the experiments.

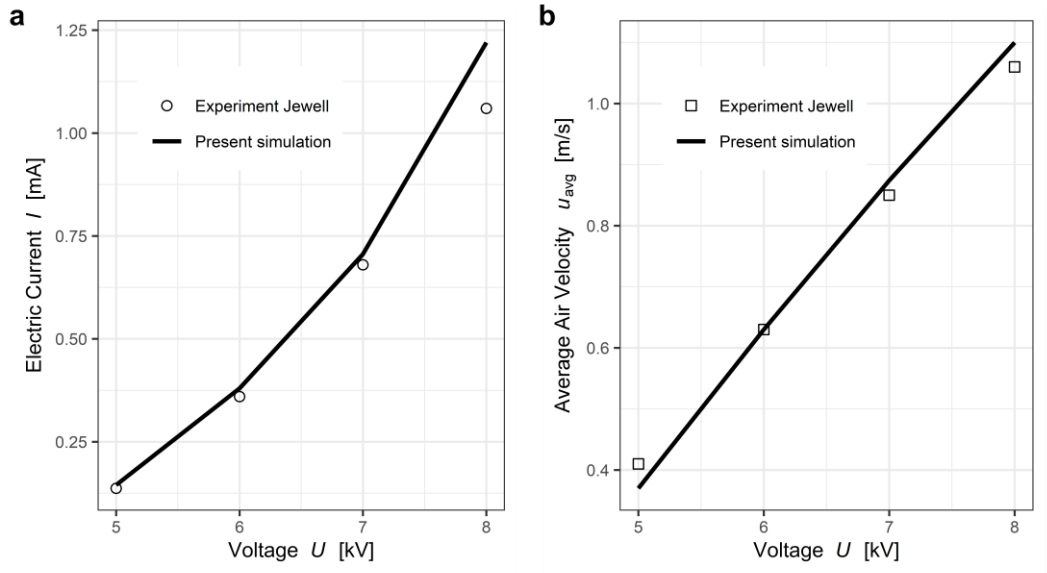

Figure 12: Comparison of numerical results with experimental data

The corresponding velocity field of the 8 kV case is shown in Figure 13. Considering a certain error margin in the experiments, we assume that our modeling approach is suitable for conducting EHD-driven flow calculations.

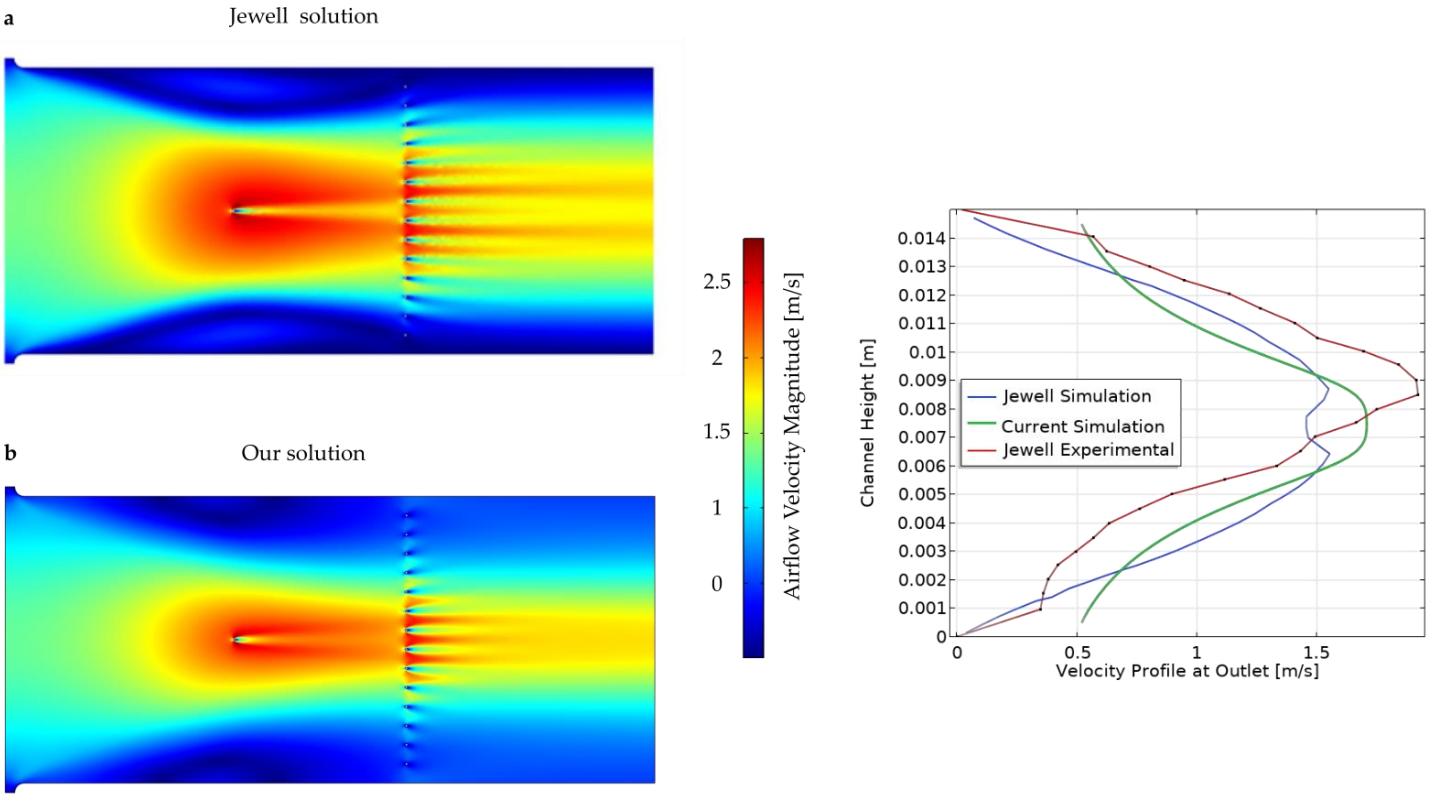

Figure 13: Comparison of flow fields at 8 kV and velocity profiles at outlet

B Analytical verification of the corona discharge model

In addition to the experimental validation of our modeling approach, we build an analytically verifiable test case for the corona discharge. It is appropriate to double-check the corona discharge mechanism as it is innovative to model the electrostatic part. The simplified 2D model for corona discharge only is shown in Figure 14A. Also, some results are shown for the space charge density in Figure 14B and an electrode close-up picture of the dimensionless electric field, which is normalized with the Peek-Kaptzov electric field E_0 according to Equation **Error! Reference source not found.**.

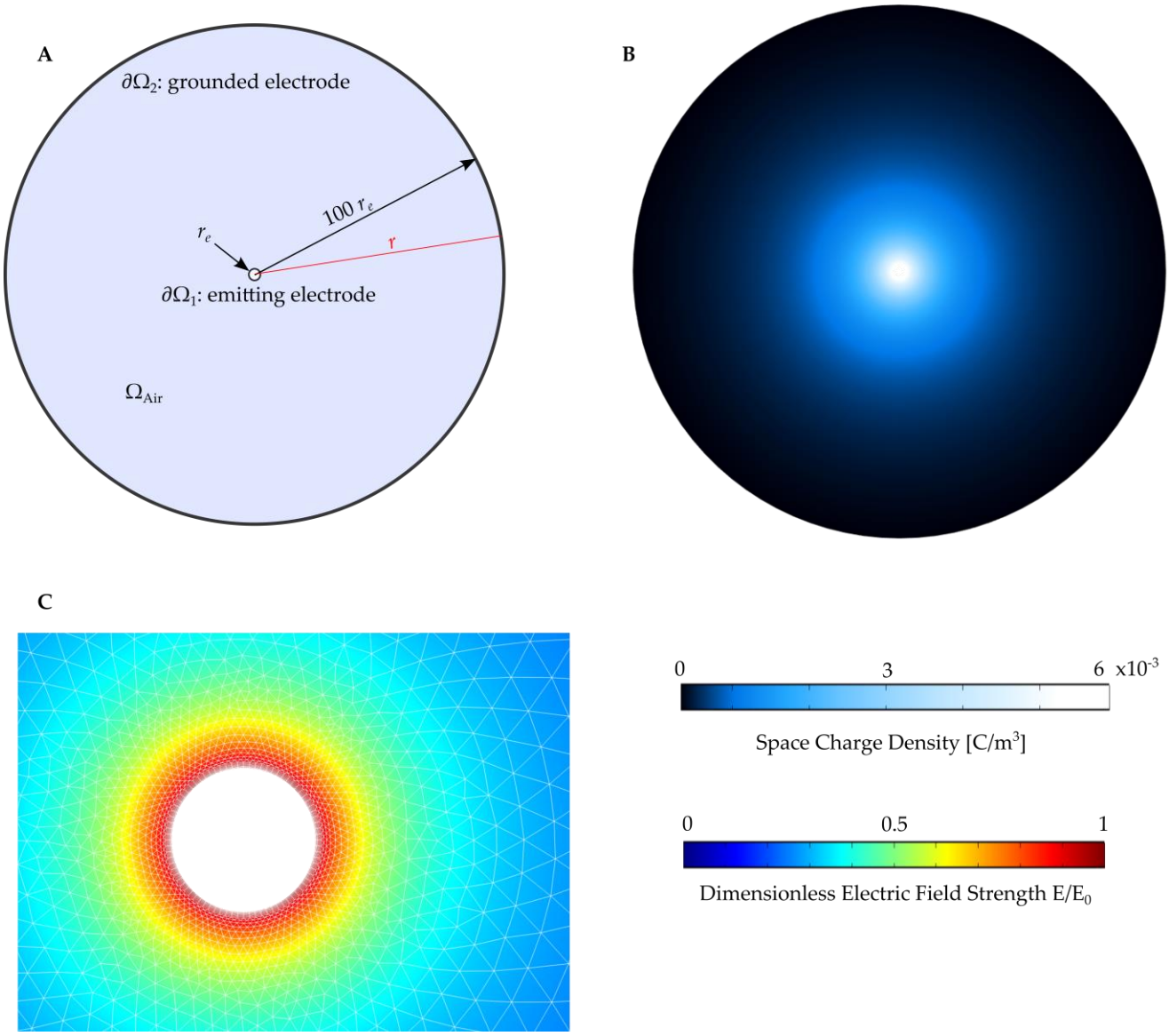

Figure 14: Setup and results of the analytical test-case setup of corona discharge

We verify the corona discharge capability by employing analytical formulas known from [24]. In dimensionless form, the electric field is

$$\frac{E(r)}{E_0} = \hat{E} = \frac{1}{\hat{r}}\sqrt{1 + \hat{A}(\hat{r}^2 - 1)} \tag{15}$$

and the corresponding dimensionless space charge density

$$\frac{\rho_{el}(r)}{\varepsilon_0 E_0 / r_e} = \hat{\rho}_{el} = \frac{\hat{A}}{\sqrt{1 + \hat{A}(\hat{r}^2 - 1)}} \tag{16}$$

with dimensionless current

$$\hat{A} = \frac{j_0 r_e}{\varepsilon_0 E_0 b} \tag{17}$$

Here, $E(r)$ is the electric field intensity along the radial axis, $\hat{r}$ is the dimensionless radius $\hat{r} = r/r_e$, ε_0 is the vacuum permittivity constant, j_0 is the current density on the electrode, and b is the ion mobility (typically in air, 1.8 x 10^{-4} $m^2/(Vs)$).

We obtain the plots in Figure 15, which compare the simulation results with the analytical solution. As can be seen, there is a perfect agreement in either case. Hence, our modeling approach with a Lagrange multiplier in Section **Error! Reference source not found.** is suitable to describe the electrostatics of EHD and of corona discharge in general.

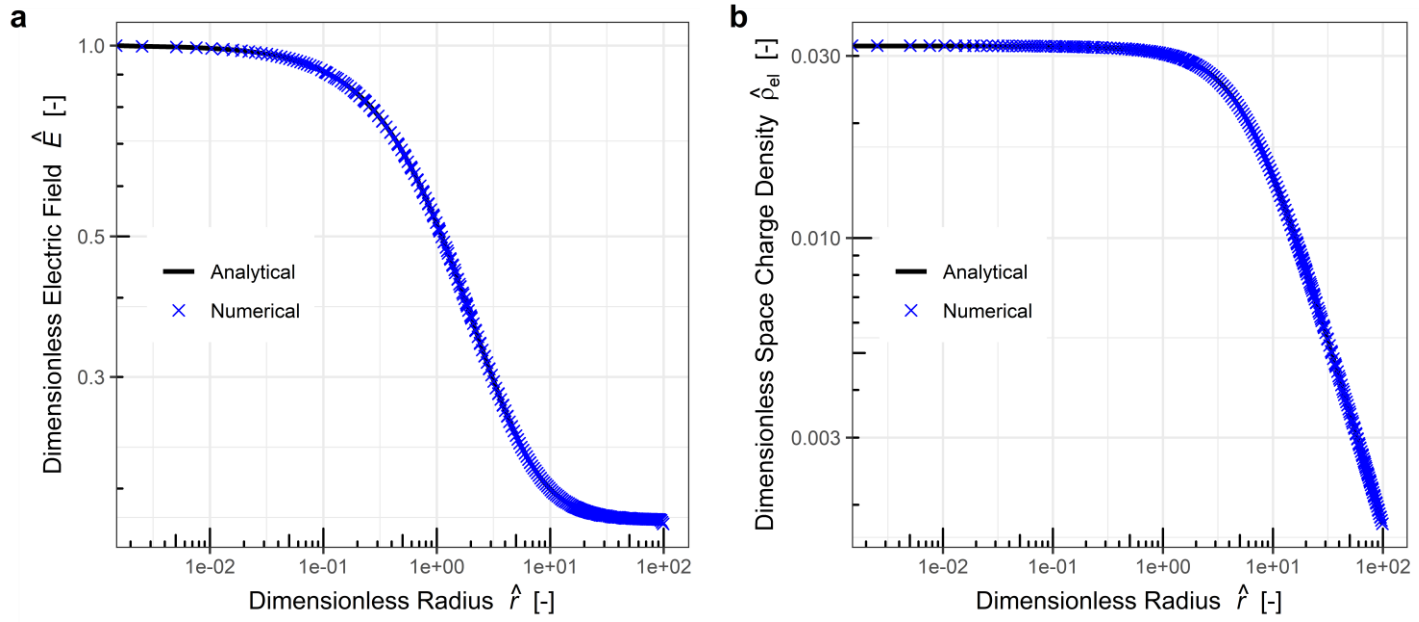

Figure 15: Analytical verification of electric field and space charge density.

C Specification of initial space charge density for single-species corona discharge modeling

Most single-species modeling approaches for corona discharge assume a constant space charge density over the entire boundary of the emitter. This is not necessary true as we know from needle electrode for example. The entire needle boundary keeps the the same voltage and to specify the single-valued initial space charge you only consider the needle tip. Then the emitting part of the needle is only the tip, but depending on the needle angle, its sides may well be ionizing the air as well. Hence, while the voltage remains constant over the entire boundary, the space charge may vary. A quick comparison to a single-species model with constant initial space charge over the entire boundary reveals that the solver tends to alter the electric potential (and hence the electric field) on the boundary to find convergence. In that sense, it is either the potential or the space charge density that shall remain constant, but not both.

We can observe that behavior in Figure 16. There, we take again Jewell's validation case [18]. When we specify a constant value for the space charge density boundary condition of the charge transport equation we see that the overall space charge in the domain propagates uniformly out of the emitter boundary until it diverges towards the grounded collector. In the bottom figure, where we employ our Lagrange Multiplier approach, we observe that the space charge propagates stronger on the side facing the collector electrode. Thus, we can assume that on emitter electrodes, there is parts that ionize more and others that ionize less.

Figure 17 shows the electric field curve and the space charge density curve on the emitter boundary. We note that using a constant initial space charge condition on the emitter forces the electric field to oscillate in order to find convergence. Whereas when a variable boundary condition for the initial space charge is employed, see Figure 17b, we obtain a spatially variable distribution which allows to maintain a constant electric field.

Depending on the electrode arrangement, a constant space charge condition presumes a strong assumption of symmetric propagation which may give rise to an essential error.

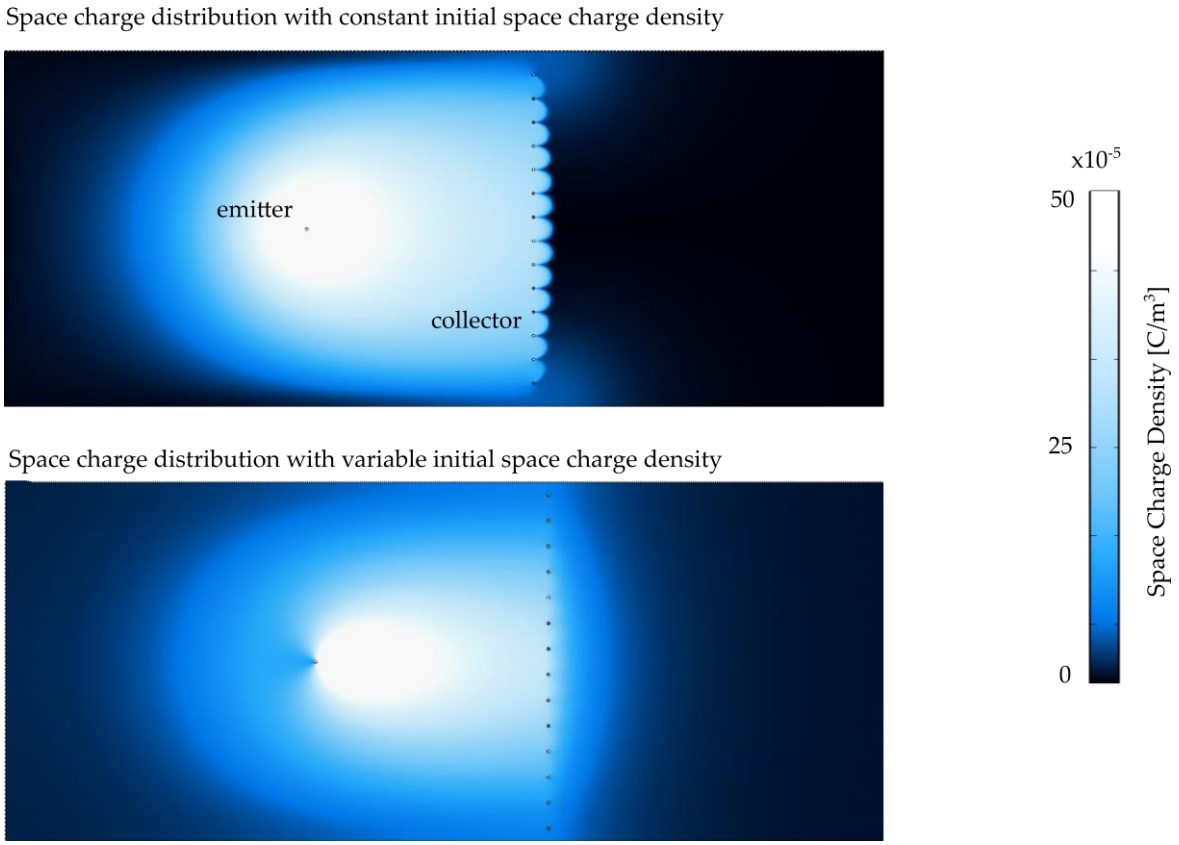

Figure 16: Comparison of constant and variable initial space charge density boundary condition for the emitter

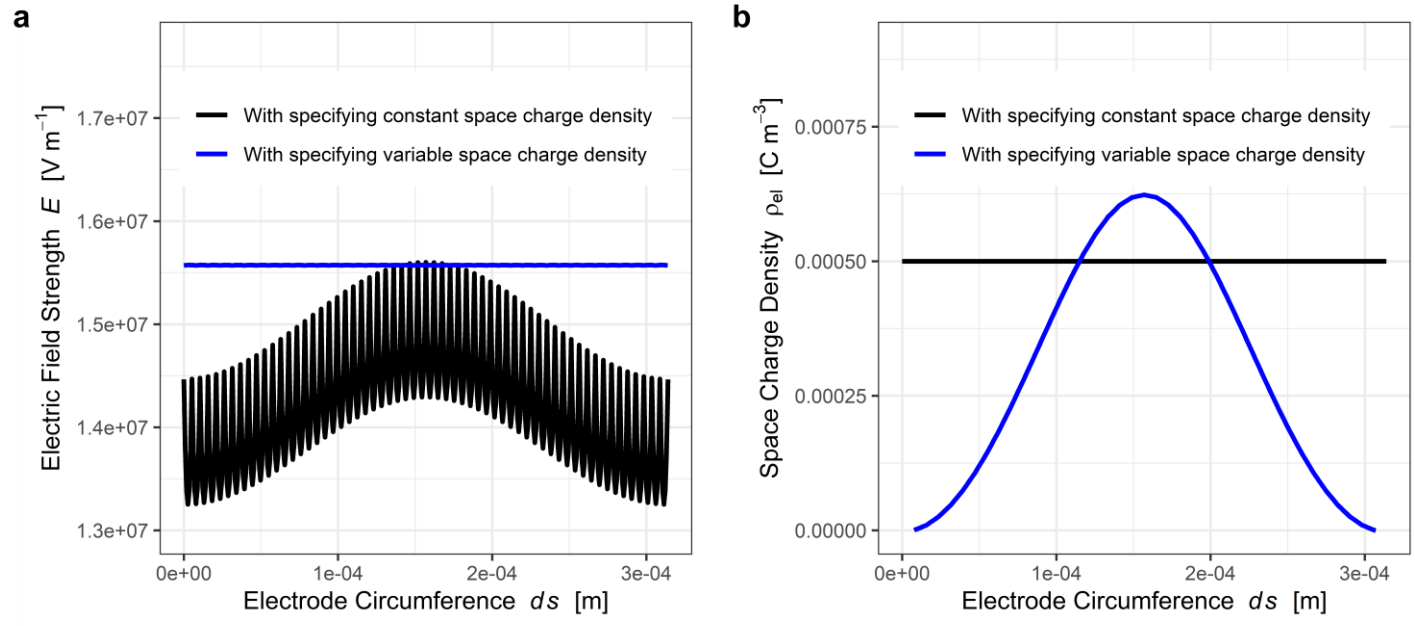

Figure 17: Distribution of electric field and space charge density on the emitter electrode circumference